Royal Aeronautical Society
8th Aircraft Structural Design Conference
3–4 October 2023, London, UK

PREPRINT

Gust Load Metrics for Multidisciplinary Design Optimization Considering Fatigue and Active Control

Bernardo Bahia Monteiro,* Carlos E. S. Cesnik,† and Ilya Kolmanovsky‡
University of Michigan, Ann Arbor, MI 48109

This paper presents a new approach for incorporate gust load alleviation (GLA) in the multidisciplinary design optimization (MDO) process. With this approach, closed-loop control considerations are incorporated into the MDO problem formulation through the inclusion of the parameterization of the sensitivity to stress transfer function of the aircraft. The parameters of this function are included as design variables and a constraint based on the Bode integral relation is imposed on it. This approach is control agnostic in the sense that it does not explicitly design a controller or its gains, which can be relegated to a later design phase. Two constraints related to the gust loads are added to the MDO problem: one for peak gust stress, based on the design envelope criterion, and the other for fatigue life under continuous turbulence. While the GLA feedback controller does not need to be designed, the optimizer designs the closed-loop sensitivity function directly. The parameterization of the sensitivity function is chosen to guarantee robustness of the closed-loop system. The use of this new approach is demonstrated by performing multidisciplinary design optimization of a flexible free-flying aircraft model subjected to gust loads. The matrix-free adjoint derivatives are verified against finite differences, and the optimum designs with and without control considerations are compared. The use of the proposed approach was able to reduce the optimal wing mass for the closed-loop design in relation to the open-loop design while still satisfying the other constraints.

I. Introduction

The first time gust load alleviation (GLA) control was considered in the multidisciplinary design optimization (MDO) of aircraft was in 1993 [1], when the structural design of a cantilevered wing was considered simultaneously with the design of a proportional integral (PI) controller that uses the measurement of the wing tip acceleration to command a control surface also located at the tip of the wing. The analysis was done in time domain and the assumed gust model was stochastic but simplified, since the turbulence input was generated based on a first order filter driven by Gaussian white noise.

An increased number of studies in this area was conducted in the last 10 to 15 years, due to renewed interest in aircraft MDO. Hunten *et al.*[2] showed results of the optimization of a blended wing-body (BWB) configuration using flap deflection for drag reduction, as well as for maneuver and gust load alleviation, considering only quasi-static gusts and maneuvers. Haghighat *et al.*[3] performed MDO of an aircraft considering a linear quadratic (LQ) controller for reducing gust loads, which are evaluated in time domain for a discrete gust. Xu and Kroo [4] performed an aerostructural design optimization of an aircraft considering a proportional derivative control system for GLA, which took the angle of attack as an input, and deflections for the two most outboard control surfaces on the wing being designed as outputs. They considered a discrete gus,t and the simulations to obtain the gust loads were performed in the time domain.

Most recently, Stanford [5] considered the design of a wingbox with trailing edge control surfaces used for GLA, including a static output feedback controller and control surface sizing into the design. To evaluate the gust loads, the turbulence model was added to the state-space representation of the airplane. No time-domain simulation was performed, instead a Lyapunov equation was solved to obtain the statistics of the stresses due to gust, which were then used to inform constraints for the optimization problem. Krengel and Hepperle [6] proposed a wing optimization problem in which the GLA controller was based on feedback of the lift coefficient, in addition to a pitch damper designed using sequential loop closure on pitch rate and angle-of-attack. They reported a 14% reduction in bending moment, with a corresponding 11.6% reduction in block fuel consumption, which was the cost function of the proposed MDO problem.

*PhD Candidate, Department of Aerospace Engineering, bbahia@umich.edu.
†Richard A. Auhll Department Chair, Clarence L. "Kelly" Johnson Professor, Department of Aerospace Engineering, cesnik@umich.edu.
‡Professor, Department of Aerospace Engineering, ilya@umich.edu.

Meanwhile, there has been much research done on the design of GLA controllers for for an already designed aircraft. In particular, Vartio *et al.* [7] designed a linear quadratic Gaussian (LQG) controller for a half BWB scaled model with multiple trailing edge control surfaces, which was then tested in free pitch and plunge at the NASA Langley's Transonic Dynamics Tunnel. The closed-loop system exhibited over 50% reduction in gust loads compared to a non-GLA controller. Zeng *et al.* [8] presented an adaptive feedforward controller capable of significantly reducing gust loads in the 2 to 20 Hz range. Dillsaver *et al.* [9] designed LQG controller considering a reduced-order flexible aircraft model and obtained expressive reduction of wing root curvature in simulation. Haghighat *et al.* [10] employed a model predictive controller (MPC) for the GLA problem, and compared its performance with a LQG controller in simulation. Pereira [11] also considered MPC-based architectures for GLA with LIDAR-based gust preview in a flexible aircraft. Ting *et al.*[12] designed and performed wind tunnel tests of preview H_2 and H_∞ controllers, reporting reduction in the wing root strains for both controllers. Fournier *et al.* [13] presented structured mixed H_2/H_∞ controller designs for gust load alleviation with the use of LIDAR measurements, and achieved 50% bending moment reduction for both discrete and continuous turbulence in simulation. Düssler *et al.* [14] designed an LQG controller that showed promising reductions in wingtip displacement of a very flexible aircraft model under continuous turbulence in linear simulations, although it presented robustness issues when tested with the non-linear simulation model.

As can be seen, there is a gap between the techniques employed to design the controllers for an already designed aircraft vs. the ones assumed in the setting of aircraft control co-design. Moreover, there is no agreed on choice of control architecture that should be used for GLA. This makes it desirable to develop an approach that guarantees the existence of a controller which gives satisfactory GLA performance for a closed-loop aircraft system without directly designing such a controller. We refer to such an approach as controller-agnostic.

This paper proposes such a controller-agnostic approach, which involves the direct optimization of the closed-loop sensitivity to stress transfer function. This transfer function reflects the combined effects of the aircraft response to control inputs and the controller. This avoids restricting the controller architecture from the beginning of the design process and leaves it for later, while guaranteeing desirable closed-loop shaping based on the designed sensitivity function [15]. The ultimate goal with this new approach is to ensure that an upper bound on the closed-loop performance informed by the airframe design exists and satisfies the design requirements, thus guaranteeing that a suitable controller exists.

The calculation of gust stresses due to continuous turbulence is performed in the frequency domain [16] and is synergistic with the classical control framework (*i.e.*, transfer functions). This procedure allows for very fast evaluation of the gust loads as compared to time domain simulations, which would have to be run for extended periods of time in order to capture rare gust events.

Notation is mostly standard, and the vectorization operation and the Kronecker product are used to to avoid dealing with tensors of order larger than two. In what follows, *(i)* I_n is the identity matrix in $\mathbb{R}^{n\times n}$; *(ii)* $\mathbf{1}$ denotes a vector in which every element is one; *(iii)* $\mathbf{0}$ denotes a vector of zeros; *(iv)* j is the complex unit ($j^2 = -1$) *(v)* $\overline{Z}$ and $|Z|$ are the element-wise complex conjugate and the element-wise absolute value of $Z \in \mathbb{C}^{m\times n}$, respectively; *(vi)* $\cdot^\top$ is the transpose operator; *(vii)* $\cdot^\mathsf{H}$ is the conjugate transpose (Hermitian) operator; *(viii)* $\cdot^{-\top}$ and $\cdot^{-H}$ denote the inverse transpose and inverse conjugate transpose, respectively; *(ix)* $\operatorname{vec}\cdot$ is the vectorization operation, which stacks the columns of a matrix to produce a column vector; *(x)* when applied to a vector, $\operatorname{diag}\cdot$ yields a diagonal matrix with the vector elements in the diagonal, and when applied to a matrix it extracts the diagonal elements into a vector; *(xi)* $\cdot \circ \cdot$ denotes the element-wise (or Hadamard) product; and *(xii)* $\cdot \otimes \cdot$ denotes the Kronecker product; *(xiii)* $\cdot^{\circ\cdot}$ denotes element-wise power (or Hadamard power). A thorough exposition on these and other topics in matrix calculus can be found in, *e.g.*, [17].

When deriving expressions for directional derivatives, we make use of the simplified notation described in [17, Section 5.16], that is, if $g(x) : U \to V$ is a vector function; U, V are vector spaces; and $\mathcal{L}(U, V)$ is the space of linear operators that map U to V, then we write $\mathrm{d}g = \frac{\partial g}{\partial x}(x)\,\mathrm{d}x$, where $\mathrm{d}x \in U$ is a direction in the input space and $\mathrm{d}g \in V$ is a direction in the output space. $\frac{\partial g}{\partial x} \in \mathcal{L}(U, V)$ is the derivative of g defined as the linear mapping that locally approximates g, *i.e.*, $\lim_{\mathrm{d}x\to\mathbf{0}} \frac{g(x+\mathrm{d}x)-g(x)-\frac{\partial g}{\partial x}(x)\,\mathrm{d}x}{\|\,\mathrm{d}x\|} = \mathbf{0}$. We also define the adjoint derivative $\left(\frac{\partial g}{\partial x}(x)\right)^* \in \mathcal{L}(V, U)$ such that $\langle \mathrm{d}g, \frac{\partial g}{\partial x}(x)\,\mathrm{d}x\rangle = \langle \left(\frac{\partial g}{\partial x}(x)\right)^* \mathrm{d}g, \mathrm{d}x\rangle$. For example, if $U = \mathbb{R}^n$ and $V = \mathbb{R}^m$, then $\frac{\partial g}{\partial x}(x) \in \mathbb{R}^{m\times n}$ and $\left(\frac{\partial g}{\partial x}(x)\right)^* = \left(\frac{\partial g}{\partial x}(x)\right)^\top$.

Some useful relations are recalled for the convenience of the reader: *(xiv)* the absolute value squared function, $|\cdot|^2 : \mathbb{C} \to \mathbb{R}_+$ is not differentiable in the complex plane because it does not satisfy the Cauchy-Riemann equations, but is differentiable when viewed as a $\mathbb{R}^2 \to \mathbb{R}_+$ mapping, *i.e.*, $|a + jb|^2 = a^2 + b^2$, where $a, b \in \mathbb{R}$, and its differential

is given by $\mathrm{d}|a+jb|^2 = 2a\,\mathrm{d}a + 2b\,\mathrm{d}b = 2\Re\left[\overline{(a+jb)}\,\mathrm{d}(a+jb)\right]$; *(xv)* the differential of the matrix inverse is given by $\mathrm{d}A^{-1} = -A^{-1}\,\mathrm{d}A\,A^{-1}$; *(xvi)* the vectorization operation is distributive over the element-wise product, *i.e.*, $\mathrm{vec}(X \circ Y) = \mathrm{vec}(X) \circ \mathrm{vec}(Y)$; *(xvii)* if u and v are vectors of the same dimension, then $u \circ v = \mathrm{diag}(u)v$; and *(xviii)* if X, Y, Z are matrices such that the product XYZ is defined, then $\mathrm{vec}(XYZ) = (Z^\top \otimes X)\,\mathrm{vec}(Y)$ —this relation is known as the "vec trick".

This paper is organized as follows. Section II presents the theoretical framework for the calculation of gust stresses and fatigue damage resulting from a stochastic turbulence input, along with their matrix-free direct and adjoint directional derivatives. Section III describes how to incorporate the sensitivity function into that formulation, and Section IV proposes a simplified MDO problem that will be solved integrating these elements. Section V presents and analyzes the resulting MDO designs, comparing open and closed-loop solutions. Finally, Section VI presents the concluding remarks.

II. Stochastic gust metrics

A. Calculations of moments of the power spectral density of stress

Consider the transfer functions from gust to normal and shear stresses at one point in the structure, given by

$$G_\sigma(s) = C_\sigma(sI - A)^{-1}B + D_\sigma \tag{1}$$

$$G_\tau(s) = C_\tau(sI - A)^{-1}B + D_\tau \tag{2}$$

where $A \in \mathbb{R}^{n_x \times n_x}$; $B \in \mathbb{R}^{n_x \times n_u}$; $C_\sigma, C_\tau \in \mathbb{R}^{n_y \times n_x}$; $D_\sigma, D_\tau \in \mathbb{R}^{n_y \times n_u}$. The tuples $(A, B, C_\sigma, D_\sigma)$ and (A, B, C_τ, D_τ), are the state space representations of the responses from gust to normal stresses and from gust to shear stresses, respectively.

The transfer functions for shear stress and gust stresses are used to calculate the magnitude of the transfer function from the gust input to the von Mises stress [18]:

$$|G_{\mathrm{VM}}(s)|^{\circ 2} = |G_\sigma(s)|^{\circ 2} + 3\,|G_\tau(s)|^{\circ 2} \tag{3}$$

The PSD of the von Mises stress is calculated by

$$\Phi_{\mathrm{VM}}(\omega) = |G_{\mathrm{VM}}(j\omega)|^{\circ 2}\,\Phi_{w_g}(\omega) \tag{4}$$

where $\Phi_{w_g}(\omega) \in \mathbb{R}^{n_u}$ is the PSD of the gust that is the input into the system, *e.g.*, given by the von Kárman power spectral density for vertical continuous turbulence (FAR §25.341):

$$\Phi_{w_G}(\omega) = U_g^2 \frac{L_w}{\pi U_\infty} \frac{1 + \frac{8}{3}(1.339 L_w \omega / U_\infty)^2}{[1 + (1.339 L_w \omega / U_\infty)^2]^{\frac{11}{6}}} \tag{5}$$

where U_g is the turbulence intensity, L_w is the turbulence scale, and U_∞ is the free stream velocity. The first two parameters can be found in the FAR.

The moments of the PSD can then be calculated by integration:

$$\lambda_m = \int_{\omega=0}^{\infty} \omega^m \Phi_{\mathrm{VM}}(\omega)\,\mathrm{d}\omega, \quad m = 0, 1, 2, 4. \tag{6}$$

Combining (1) to (4) and (6), it follows that

$$\lambda_m = \int_{\omega=0}^{\infty} \omega^m \left(|C_\sigma(j\omega I - A)^{-1}B + D_\sigma|^{\circ 2} + 3|C_\tau(j\omega I - A)^{-1}B + D_\tau|^{\circ 2}\right) \Phi_{w_g}(\omega)\,\mathrm{d}\omega \tag{7}$$

For this integral to converge, it suffices that the integrand is bounded by $C^*\omega^{-x}$, for some $C^*, x \in \mathbb{R}$, $x > 1$, and for large values of ω. If the term $\Phi_{w_g}(\omega)$ represents the von Kármán power spectral distribution for turbulence in the vertical direction, it decays proportionally to $\omega^{-5/3}$ at high frequencies, which means that the moment of order m will be finite if the relative degree of each gust-to-stress transfer function is greater or equal to $\sqrt{m}$.

B. Computation of derivatives of the PSD moments

The following matrices of frequency response functions are introduced in order to keep the expressions for the derivatives of (7) compact:

$$\mathcal{X}(\omega) = (j\omega I - A)^{-1}B \qquad \in \mathbb{R}^{n_x \times n_u} \tag{8a}$$
$$\mathcal{Y}_\sigma(\omega) = C_\sigma(j\omega I - A)^{-1} \qquad \in \mathbb{R}^{n_y \times n_x} \tag{8b}$$
$$\mathcal{Y}_\tau(\omega) = C_\tau(j\omega I - A)^{-1} \qquad \in \mathbb{R}^{n_y \times n_x} \tag{8c}$$
$$G_\sigma(\omega) = C_\sigma(j\omega I - A)^{-1}B + D_\sigma \qquad \in \mathbb{R}^{n_y \times n_u} \tag{8d}$$
$$G_\tau(\omega) = C_\tau(j\omega I - A)^{-1}B + D_\tau \qquad \in \mathbb{R}^{n_y \times n_u} \tag{8e}$$

Differentiating (7) with the use of (xiv) and (xv), and swapping the order of the integration with differentiation (the precise assumptions under which this is possible are presented in *e.g.*, [19]):

$$\begin{aligned} \mathrm{d}\lambda_m = \int_{\omega=0}^{\infty} \omega^m \Re\Big[& 2\overline{G_\sigma}(\omega) \circ \big(\mathrm{d}C_\sigma \mathcal{X}(\omega) + \mathcal{Y}_\sigma(\omega)\,\mathrm{d}A\ \mathcal{X}(\omega) + \mathcal{Y}_\sigma(\omega)\,\mathrm{d}B + \mathrm{d}D_\sigma\big) \\ & + 6\overline{G_\tau}(\omega) \circ \big(\mathrm{d}C_\tau \mathcal{X}(\omega) + \mathcal{Y}_\tau(\omega)\,\mathrm{d}A\ \mathcal{X}(\omega) + \mathcal{Y}_\tau(\omega)\,\mathrm{d}B + \mathrm{d}D_\tau\big)\Big] \Phi_{w_g}(\omega)\,\mathrm{d}\omega \end{aligned} \tag{9}$$

This equation allows the calculation of the directional derivatives at a point $(A, B, C_\sigma, C_\tau, D_\sigma, D_\tau)$ given directions for the inputs, *i.e.*, values for $\mathrm{d}A$, $\mathrm{d}B$, $\mathrm{d}C_\sigma$, $\mathrm{d}C_\tau$, $\mathrm{d}D_\sigma$, and $\mathrm{d}D_\tau$. Note that $\mathrm{d}\lambda_m$ in (9) is linear in the differentials, which are independent of the integration variable ω, allowing it to be written as

$$\mathrm{d}\lambda_m = \frac{\partial \lambda_m}{\partial C_\sigma}\mathrm{d}C_\sigma + \frac{\partial \lambda_m}{\partial C_\tau}\mathrm{d}C_\tau + \frac{\partial \lambda_m}{\partial A}\mathrm{d}A + \frac{\partial \lambda_m}{\partial B}\mathrm{d}B + \frac{\partial \lambda_m}{\partial D_\sigma}\mathrm{d}D_\sigma + \frac{\partial \lambda_m}{\partial D_\tau}\mathrm{d}D_\tau \tag{10}$$

where the Jacobians are third-order tensors.

This equation can be vectorized by applying the vec operator to both sides of the equal sign and using the properties presented in Section I, starting with the "vec-trick" (xviii):

$$\begin{aligned} \mathrm{vec}\,\mathrm{d}\lambda_m = \int_{\omega=0}^{\infty} \omega^m & \big(\Phi_{w_g}(\omega)^\top \otimes I_{n_y}\big) \\ & \mathrm{vec}\Big\{ \Re\Big[2\overline{G_\sigma}(\omega) \circ \big(\mathrm{d}C_\sigma \mathcal{X}(\omega) + \mathcal{Y}_\sigma(\omega)\,\mathrm{d}A\ \mathcal{X}(\omega) + \mathcal{Y}_\sigma(\omega)\,\mathrm{d}B + \mathrm{d}D_\sigma\big) \\ & \quad + 6\overline{G_\tau}(\omega) \circ \big(\mathrm{d}C_\tau \mathcal{X}(\omega) + \mathcal{Y}_\tau(\omega)\,\mathrm{d}A\ \mathcal{X}(\omega) + \mathcal{Y}_\tau(\omega)\,\mathrm{d}B + \mathrm{d}D_\tau\big)\Big]\Big\}\,\mathrm{d}\omega \end{aligned} \tag{11}$$

Using the fact that vec is distributive over the element-wise product (xvi):

$$\begin{aligned} \mathrm{vec}\,\mathrm{d}\lambda_m = \int_{\omega=0}^{\infty} \omega^m & \big(\Phi_{w_g}(\omega)^\top \otimes I_{n_y}\big) \\ & \Re\Big\{ 2\,\mathrm{vec}\,\overline{G_\sigma}(\omega) \circ \Big[\big(\mathcal{X}(\omega)^\top \otimes I_{n_y}\big)\,\mathrm{vec}\,\mathrm{d}C_\sigma + \big(\mathcal{X}(\omega)^\top \otimes \mathcal{Y}_\sigma(\omega)\big)\,\mathrm{vec}\,\mathrm{d}A \\ & \qquad + \big(I_{n_u} \otimes \mathcal{Y}_\sigma(\omega)\big)\,\mathrm{vec}\,\mathrm{d}B + \mathrm{vec}\,\mathrm{d}D_\sigma\Big] \\ & \quad + 6\,\mathrm{vec}\,\overline{G_\tau}(\omega) \circ \Big[\big(\mathcal{X}(\omega)^\top \otimes I_{n_y}\big)\,\mathrm{vec}\,\mathrm{d}C_\tau + \big(\mathcal{X}(\omega)^\top \otimes \mathcal{Y}_\tau(\omega)\big)\,\mathrm{vec}\,\mathrm{d}A \\ & \qquad + \big(I_{n_u} \otimes \mathcal{Y}_\tau(\omega)\big)\,\mathrm{vec}\,\mathrm{d}B + \mathrm{vec}\,\mathrm{d}D_\tau\Big]\Big\}\,\mathrm{d}\omega \end{aligned} \tag{12}$$

Applying the property that the element-wise product of two vectors is equal to multiplying a vector by the matrix with

the elements of the other in the diagonal (xvii):

$$\begin{aligned}\operatorname{vec} \mathrm{d}\lambda_m = \int_{\omega=0}^{\infty} \omega^m \left(\Phi_{w_g}(\omega)^\top \otimes I_{n_y}\right) \\ \Re\Big\{ 2\operatorname{diag}\left(\operatorname{vec}\overline{G_\sigma}(\omega)\right)\Big[\left(\chi(\omega)^\top \otimes I_{n_y}\right)\operatorname{vec}\mathrm{d}C_\sigma + \left(\chi(\omega)^\top \otimes \psi_\sigma(\omega)\right)\operatorname{vec}\mathrm{d}A \\ + \left(I_{n_u} \otimes \psi_\sigma(\omega)\right)\operatorname{vec}\mathrm{d}B + \operatorname{vec}\mathrm{d}D_\sigma\Big] \\ + 6\operatorname{diag}\left(\operatorname{vec}\overline{G_\tau}(\omega)\right)\Big[\left(\chi(\omega)^\top \otimes I_{n_y}\right)\operatorname{vec}\mathrm{d}C_\tau + \left(\chi(\omega)^\top \otimes \psi_\tau(\omega)\right)\operatorname{vec}\mathrm{d}A \\ + \left(I_{n_u} \otimes \psi_\tau(\omega)\right)\operatorname{vec}\mathrm{d}B + \operatorname{vec}\mathrm{d}D_\tau\Big]\Big\}\,\mathrm{d}\omega \end{aligned} \tag{13}$$

The linear caracter of this relation can be made explicit by writing it as

$$\begin{aligned}\operatorname{vec}\mathrm{d}\lambda_m = \frac{\partial \operatorname{vec}(\lambda_m)}{\partial \operatorname{vec}(C_\sigma)}\operatorname{vec}\mathrm{d}C_\sigma + \frac{\partial \operatorname{vec}(\lambda_m)}{\partial \operatorname{vec}(C_\tau)}\operatorname{vec}\mathrm{d}C_\tau + \frac{\partial \operatorname{vec}(\lambda_m)}{\partial \operatorname{vec}(A)}\operatorname{vec}\mathrm{d}A \\ + \frac{\partial \operatorname{vec}(\lambda_m)}{\partial \operatorname{vec}(B)}\operatorname{vec}\mathrm{d}B + \frac{\partial \operatorname{vec}(\lambda_m)}{\partial \operatorname{vec}(D_\sigma)}\operatorname{vec}\mathrm{d}D_\sigma + \frac{\partial \operatorname{vec}(\lambda_m)}{\partial \operatorname{vec}(D_\tau)}\operatorname{vec}\mathrm{d}D_\tau \end{aligned} \tag{14}$$

where the Jacobians of the vectorized input-output pairs are given by:

$$\frac{\partial \operatorname{vec}(\lambda_m)}{\partial \operatorname{vec}(C_\sigma)} = \int_{\omega=0}^{\infty} \omega^m \left(\Phi_{w_g}(\omega)^\top \otimes I_{n_y}\right)\Re\left[2\operatorname{diag}\left(\operatorname{vec}\overline{G_\sigma}(\omega)\right)\left(\chi(\omega)^\top \otimes I_{n_y}\right)\right]\mathrm{d}\omega \tag{15a}$$

$$\frac{\partial \operatorname{vec}(\lambda_m)}{\partial \operatorname{vec}(C_\tau)} = \int_{\omega=0}^{\infty} \omega^m \left(\Phi_{w_g}(\omega)^\top \otimes I_{n_y}\right)\Re\left[6\operatorname{diag}\left(\operatorname{vec}\overline{G_\tau}(\omega)\right)\left(\chi(\omega)^\top \otimes I_{n_y}\right)\right]\mathrm{d}\omega \tag{15b}$$

$$\begin{aligned}\frac{\partial \operatorname{vec}(\lambda_m)}{\partial \operatorname{vec}(A)} = \int_{\omega=0}^{\infty} \omega^m \left(\Phi_{w_g}(\omega)^\top \otimes I_{n_y}\right)\Re\Big[2\operatorname{diag}\left(\operatorname{vec}\overline{G_\sigma}(\omega)\right)\left(\chi(\omega)^\top \otimes \psi_\sigma(\omega)\right) \\ + 6\operatorname{diag}\left(\operatorname{vec}\overline{G_\tau}(\omega)\right)\left(\chi(\omega)^\top \otimes \psi_\tau(\omega)\right)\Big]\mathrm{d}\omega \end{aligned} \tag{15c}$$

$$\begin{aligned}\frac{\partial \operatorname{vec}(\lambda_m)}{\partial \operatorname{vec}(B)} = \int_{\omega=0}^{\infty} \omega^m \left(\Phi_{w_g}(\omega)^\top \otimes I_{n_y}\right)\Re\Big[2\operatorname{diag}\left(\operatorname{vec}\overline{G_\sigma}(\omega)\right)\left(I_{n_u} \otimes \psi_\sigma(\omega)\right) \\ + 6\operatorname{diag}\left(\operatorname{vec}\overline{G_\tau}(\omega)\right)\left(I_{n_u} \otimes \psi_\tau(\omega)\right)\Big]\mathrm{d}\omega \end{aligned} \tag{15d}$$

$$\frac{\partial \operatorname{vec}(\lambda_m)}{\partial \operatorname{vec}(D_\sigma)} = \int_{\omega=0}^{\infty} \omega^m \left(\Phi_{w_g}(\omega)^\top \otimes I_{n_y}\right)\Re\left[2\operatorname{diag}\left(\operatorname{vec}\overline{G_\sigma}(\omega)\right)\right]\mathrm{d}\omega \tag{15e}$$

$$\frac{\partial \operatorname{vec}(\lambda_m)}{\partial \operatorname{vec}(D_\tau)} = \int_{\omega=0}^{\infty} \omega^m \left(\Phi_{w_g}(\omega)^\top \otimes I_{n_y}\right)\Re\left[6\operatorname{diag}\left(\operatorname{vec}\overline{G_\tau}(\omega)\right)\right]\mathrm{d}\omega \tag{15f}$$

The adjoint operatosr in the vectorized basis are the transpose of the direct operators, shown in (15). They can be

Table 1 Dimensions of explicit and matrix-free derivatives

	Direct	Jacobian	Adjoint
$\frac{\partial \lambda_m}{\partial C_\sigma}$	$\mathbb{R}^{n_y \times n_x} \to \mathbb{R}^{n_y}$	$\mathbb{R}^{n_y \times n_y \times n_x}$	$\mathbb{R}^{n_y} \to \mathbb{R}^{n_y \times n_x}$
$\frac{\partial \lambda_m}{\partial C_\tau}$	$\mathbb{R}^{n_y \times n_x} \to \mathbb{R}^{n_y}$	$\mathbb{R}^{n_y \times n_y \times n_x}$	$\mathbb{R}^{n_y} \to \mathbb{R}^{n_y \times n_x}$
$\frac{\partial \lambda_m}{\partial A}$	$\mathbb{R}^{n_x \times n_x} \to \mathbb{R}^{n_y}$	$\mathbb{R}^{n_y \times n_x \times n_x}$	$\mathbb{R}^{n_y} \to \mathbb{R}^{n_x \times n_x}$
$\frac{\partial \lambda_m}{\partial B}$	$\mathbb{R}^{n_x \times n_u} \to \mathbb{R}^{n_y}$	$\mathbb{R}^{n_y \times n_x \times n_y}$	$\mathbb{R}^{n_y} \to \mathbb{R}^{n_x \times n_u}$
$\frac{\partial \lambda_m}{\partial D_\sigma}$	$\mathbb{R}^{n_y \times n_u} \to \mathbb{R}^{n_y}$	$\mathbb{R}^{n_y \times n_y \times n_u}$	$\mathbb{R}^{n_y} \to \mathbb{R}^{n_y \times n_u}$
$\frac{\partial \lambda_m}{\partial D_\tau}$	$\mathbb{R}^{n_y \times n_u} \to \mathbb{R}^{n_y}$	$\mathbb{R}^{n_y \times n_y \times n_u}$	$\mathbb{R}^{n_y} \to \mathbb{R}^{n_y \times n_u}$

evaluated and written in the original (not-vectorized) basis, yielding the following matrix-free adjoint equations:

$$\left(\frac{\partial \lambda_m}{\partial C_\sigma}\right)^* \mathrm{d}\lambda_m = \int_{\omega=0}^{\infty} \omega^m \Re\left\{\left[2\overline{G_\sigma}(\omega) \circ \left(\mathrm{d}\lambda_m \, \Phi_{w_g}(\omega)^\top\right)\right] \chi(\omega)^\top\right\} \mathrm{d}\omega \tag{16a}$$

$$\left(\frac{\partial \lambda_m}{\partial C_\tau}\right)^* \mathrm{d}\lambda_m = \int_{\omega=0}^{\infty} \omega^m \Re\left\{\left[6\overline{G_\tau}(\omega) \circ \left(\mathrm{d}\lambda_m \, \Phi_{w_g}(\omega)^\top\right)\right] \chi(\omega)^\top\right\} \mathrm{d}\omega \tag{16b}$$

$$\begin{aligned}\left(\frac{\partial \lambda_m}{\partial A}\right)^* \mathrm{d}\lambda_m = \int_{\omega=0}^{\infty} \omega^m \Re\Big\{&\psi_\sigma(\omega)^\top \left[2\overline{G_\sigma}(\omega) \circ \left(\mathrm{d}\lambda_m \Phi_{w_g}(\omega)^\top\right)\right] \chi(\omega)^\top \\ &+ \psi_\tau(\omega)^\top \left[6\overline{G_\tau}(\omega) \circ \left(\mathrm{d}\lambda_m \Phi_{w_g}(\omega)^\top\right)\right] \chi(\omega)^\top\Big\} \mathrm{d}\omega\end{aligned} \tag{16c}$$

$$\begin{aligned}\left(\frac{\partial \lambda_m}{\partial B}\right)^* \mathrm{d}\lambda_m = \int_{\omega=0}^{\infty} \omega^m \Re\Big\{&\psi_\sigma(\omega)^\top \left[2\overline{G_\sigma}(\omega) \circ \left(\mathrm{d}\lambda_m, \Phi_{w_g}(\omega)^\top\right)\right] \\ &+ \psi_\tau(\omega)^\top \left[6\overline{G_\tau}(\omega) \circ \left(\mathrm{d}\lambda_m \, \Phi_{w_g}(\omega)^\top\right)\right]\Big\} \mathrm{d}\omega\end{aligned} \tag{16d}$$

$$\left(\frac{\partial \lambda_m}{\partial D_\sigma}\right)^* \mathrm{d}\lambda_m = \int_{\omega=0}^{\infty} \omega^m \Re\left[2\overline{G_\sigma}(\omega) \circ \left(\mathrm{d}\lambda_m \Phi_{w_g}(\omega)^\top\right)\right] \mathrm{d}\omega \tag{16e}$$

$$\left(\frac{\partial \lambda_m}{\partial D_\tau}\right)^* \mathrm{d}\lambda_m = \int_{\omega=0}^{\infty} \omega^m \Re\left[6\overline{G_\tau}(\omega) \circ \left(\mathrm{d}\lambda_m \Phi_{w_g}(\omega)^\top\right)\right] \mathrm{d}\omega \tag{16f}$$

The direct derivatives, (9), allow the calculation of the directional derivative of the function given a direction in the input space, while the adjoint derivatives, (16), allow the calculation of this directional derivative given a direction in the output space. They can be used to calculate the total derivatives for the optimization problem without forming the potentially very big Jacobian matrices of (15). Table 1 summarizes the sizes of the matrices involved in these different forms of obtaining derivatives.

C. Peak stress metric

To constrain the peak stress to which the wingbox is subjected to under continuous turbulence, the continuous turbulence design criterium from the FAR §25.341 is employed, considering the transfer function from gust to stress as suggested in the AC 25.341-1§6.3.2.6.4. See also [16] for a more detailed description of the method. This calculation yields the peak gust stress, σ_{gust}, as a function of the 1-g stress, $\sigma_{\text{1-g}}$, and the turbulence intensity, σ_{gust}, which is a design parameter specified by the FAR. All stresses are considered to be von Mises aggregated stresses. The relation* is given by:

$$\sigma_{\text{gust}} = \sqrt{\lambda_0} U_{\text{gust}} \tag{17}$$

*The FAR notation for $\sqrt{\lambda_0}$ is $\overline{A}$

where λ_0 is calculated by (7) considering the normalized von Kármán power spectral density given by (5) with $U_g = 0$. The total stress is calculated by summing the 1-g straight and level flight stress to the peak gust stress, in order to calculate the margin of safety (MS), given by

$$\text{MS} = \frac{\sigma_{\text{allowable}}}{|\sigma_{\text{gust}} + \sigma_{\text{1-g}}|} - 1.5 \tag{18}$$

where $\sigma_{\text{allowable}}$ is the allowable stress for the application. The margin of safety of the peak gust stress is constrained to be non-negative, *i.e.*,

$$\text{MS} \geq 0 \tag{19}$$

D. Fatigue metric

When formulating an MDO problem that involves gust loads, it is important to incorporate a fatigue constraint to correctly evaluate designs with large stress power at high frequency bands. Even if the peak stress to which these designs are exposed is safe, they may be subjected to a high number of stress cycles that will lead to fatigue damage.

The most widely used method to calculate fatigue damage is based on the Palmgreen-Miner rule [20, 21] combined with the rainflow count of cycles in the stress time history to calculate the damage experienced by the material over time (see *e.g.*, [22]). Since the approach herein in the frequency domain, it would be very costly to generate a representative time signal of the stress (*e.g.*, by designing a filter driven by white noise). Instead, the preferred approach is to use Dirklik's empirical method for approximating the rate of damage due to gust [23], and then constraining this damage rate by a limit based on the expected flight hours in turbulence for the lifetime of the airframe. Dirklik's method has been shown to provide good agreement with the time-domain rainflow counting analysis [24].

This method uses the moments of order 0, 1, 2 and 4 of the stress PSD to estimate the mean damage rate of the rainflow count method denoted by $\dot{D}^{DK}_{RFC}$. The von Mises aggregated stresses are considered as proposed by [18]. The equations that define Dirklik's method are reproduced below, for a single point in the structure (*i.e.*, $\lambda_0, \lambda_1, \lambda_2, \lambda_4 \in \mathbb{R}$)

$$\dot{D}^{DK}_{RFC} = \frac{\nu_p}{C}\sqrt{\lambda_0}\left[D_1 Q^k \Gamma(1+k) + 2^{k/2}\Gamma(1+k/2)(D_2|R|^k + D_3)\right] \tag{20}$$

where:

$$\begin{aligned}
\nu_0 &= \frac{1}{2\pi}\sqrt{\frac{\lambda_2}{\lambda_0}} & \nu_p &= \frac{1}{2\pi}\sqrt{\frac{\lambda_4}{\lambda_2}} & \alpha_2 &= \frac{\lambda_2}{\sqrt{\lambda_0\lambda_4}} \\
x_m &= \frac{\lambda_1}{\lambda_0}\sqrt{\frac{\lambda_2}{\lambda_4}} & D_1 &= \frac{2(x_m - \alpha_2^2)}{1+\alpha_2^2} & D_2 &= \frac{1-\alpha_2-D_1+D_1^2}{1-R} \\
D_3 &= 1 - D_1 - D_2 & Q &= \frac{1.25(\alpha_2 - D_3 - D_2 R)}{D_1} & R &= \frac{\alpha_2 - x_m - D_1^2}{1-\alpha_2-x_m-D_1+D_1^2}
\end{aligned} \tag{21}$$

The parameters ν_0 and ν_p correspond to the frequency of zero crossing and frequency of peaks of the random signal, respectively, $\Gamma(\cdot)$ is the Gamma function, and C and k are the parameters of the material's S-N curve expressed as $N = C\sigma^{-k}$, which can be obtained from, *e.g.*, MIL-HDBK-5J with unity stress ratio.

The expected life in fatigue is then given by

$$\mathbb{E}[\text{fatigue life}] = \frac{1}{\dot{D}^{DK}_{RFC}} \tag{22}$$

A safety factor of 3 is usually applied to this value, and an additional factor of 1.5 is applied to allow for the variability of loading between different aircraft of the same type [25]. The appropriate gust intensity for using with the von Kármán model when doing the fatigue life calculation described can be obtained from, *e.g.*, MIL-HDBK-1797.

It was found that the optimization converges better when the logarithm of the expected fatigue life is considered, i.e. a constraint is imposed on

$$\log_{10}\mathbb{E}[\text{fatigue life}] = \log_{10}[1/\dot{D}^{DK}_{RFC}] \tag{23}$$

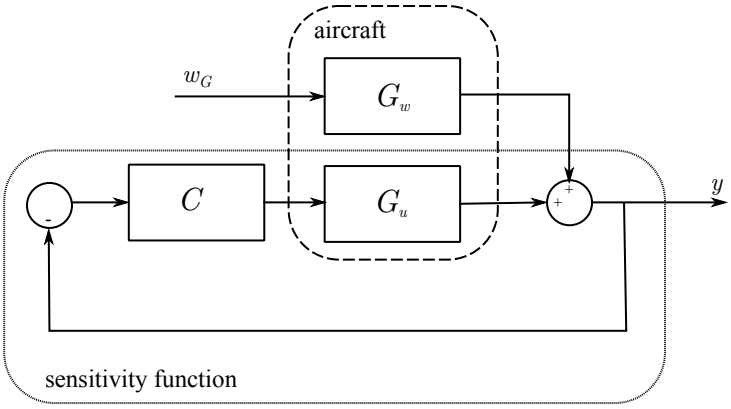

Fig. 1 Block diagram of the aircraft closed-loop system partition with a GLA controller.

E. Flutter metric

In order to ensure that the system is open-loop stable (flutter-free), the approach proposed in [26] is adopted. It consists of constraining the real part of the eigenvalues of the A matrix (poles of the system) to be less than zero. These constraints are aggregated using the Kreisselmeier-Steinhauser (KS) function [27–29] to achieve greater numerical efficiency in the calculation of the derivatives in the adjoint mode, as well as removing the need for mode tracking. The derivative of the eigenvalues with respect to the A matrix can be obtained by the method proposed by Nelson [30]: let $A \in \mathbb{R}^{n_x \times n_x}$ be diagonalizable, *i.e.*, $A = V\Lambda V^{-1}$, where Λ is the diagonal matrix of eigenvalues and V is the matrix of eigenvectors. Then:

$$\mathrm{d}\Lambda = V^{-1}\,\mathrm{d}A V \tag{24}$$

The vec-trick (xviii) can be applied to this equation

$$\operatorname{vec}\mathrm{d}\Lambda = (V^{\top} \otimes V^{-1})\operatorname{vec}\mathrm{d}A \tag{25}$$

From (25), the adjoint vectorized Jacobian can be computed by taking its conjugate transpose

$$\left(\frac{\partial \operatorname{vec}\Lambda}{\partial \operatorname{vec} A}\right)^{*} \operatorname{vec}\mathrm{d}\Lambda = (V^{\top} \otimes V^{-1})^{\mathsf{H}} \operatorname{vec}\mathrm{d}\Lambda = (\overline{V} \otimes V^{-\mathsf{H}}) \operatorname{vec}\mathrm{d}\Lambda = \operatorname{vec}(V^{-\mathsf{H}}\,\mathrm{d}\Lambda V^{\mathsf{H}}) \tag{26}$$

Therefore,

$$\left(\frac{\partial \Lambda}{\partial A}\right)^{*} \mathrm{d}\Lambda = V^{-\mathsf{H}}\,\mathrm{d}\Lambda V^{\mathsf{H}} \tag{27}$$

III. Sensitivity function approach

A. Calculation of closed loop moments of the stress PSD

The new approach starts with separating the aircraft plant into a gust response part and a control response part, as shown in Figure 1, where $K(s)$ denotes the controller, $G_u(s)$ denotes the control input response part of the plant, and $G_w(s)$ is the disturbance response part of the plant. The feedback loop, consisting of the controller and control response parts of the plant, is then considered and characterized by its sensitivity function,

$$S(s) = \Big(I_{n_y} + G_u(s)K(s)\Big)^{-1} \tag{28}$$

The sensitivity function represents the closed-loop response to a disturbance applied at the plant's output, in this case the von Mises stress due to gust. By parameterizing it and using the parameters as additional design variables in the MDO problem, which incorporates the gust constraints described in Section II, it is possible to assess the impact of the GLA system on the airframe optimal design, without explicit controller design. Specifically, (6) is modified to account for the assumed sensitivity function, which acts as a filter at the output of G_w, yielding

$$\lambda_m = \int_{\omega=0}^{\infty} \omega^m |S(j\omega)|^{\circ 2} \Phi_{\mathrm{VM}}(\omega)\,\mathrm{d}\omega, \quad m = 0, 1, 2, 4 \tag{29}$$

B. The Bode integral relation

Assuming a linear time invariant (LTI) plant and controller without time delays, the sensitivity function must satisfy the Bode integral relation:

$$\int_{\omega=0}^{\infty} \log|S(j\omega)|\mathrm{d}\omega = \pi \sum_{k=1}^{n_u} \mathrm{Re}(p_k) \tag{30}$$

for a single-input single-output (SISO) system [31, 32], or

$$\int_{\omega=0}^{\infty} \log|\det S(j\omega)|\mathrm{d}\omega = \pi \sum_{k=1}^{n_u} \mathrm{Re}(p_k) \tag{31}$$

for a multiple-input multiple-output (MIMO) system (see, *e.g.*, [33] and references therein), where in both cases p_k, $k = 1, \ldots, n_u$, are the open-loop poles in the open right half plane.

The Bode integral relation is a fundamental control limitation that captures the effects of finite actuation bandwidth and reflects the inherent difficulty of stabilizing an unstable plant. It ensures that any reduction in sensitivity over some frequency range is accompanied by an increase in sensitivity at other frequencies (the water bed effect),

For simplicity, each gust-to-stress transfer function is considered as its own SISO system and (30) is added to the problem as an aditional constraint. A single sensitivity function is designed for all points where the stress is evaluated. For a stable plant, which is the case considered in this paper due to the flutter constraint, this is equivalent to assuming a diagonal structure in the MIMO matrix of senstivity functions, with repeated entries in the diagonal.

Finally, robustness constraints can be imposed on the sensitivity function. For the case of a single-input single-output (SISO) system, the peak of the sensitivity function can be bounded through the parameterization, which in turn provides bounds to the gain and phase margins [34, 35].

Specifically, peak of the magnitude of the sensitivity function is related to the robustness of the closed-loop system, specifically, the sensitivity peak magnitude M_S is the minimum distance between the Nyquist curve and the critical point -1 [33]. The following bounds on the gain margin (GM) and on the phase margin (PM) can be stated in terms of M_S:

$$\mathrm{GM} \geq \frac{M_S}{M_S - 1}, \qquad \mathrm{PM} \geq 2\sin^{-1}\left(\frac{1}{2M_S}\right). \tag{32}$$

For example, $M_S \leq 2$ guarantees a gain margin of at least 6 dB and phase margin of at least 29°, which are usual requirements for control design.

C. Derivatives of PSD moments with respect to the sensitivity function

Differentiating (29) yields

$$\mathrm{d}\lambda_m = \int_{\omega=0}^{\infty} \omega^m \left\{\mathrm{d}\left[|S(j\omega)|^{\circ 2}\right]\Phi_{\mathrm{VM}}(\omega) + |S(j\omega)|^{\circ 2}\,\mathrm{d}\Phi_{\mathrm{VM}}(\omega)\right\}\mathrm{d}\omega \tag{33}$$

from which the direct matrix-free directional derivative can be obtained:

$$\frac{\partial\lambda_m}{\partial|S(j\omega)|^{\circ 2}}\,\mathrm{d}\left[|S(j\omega)|^{\circ 2}\right] = \int_{\omega=0}^{\infty} \omega^m\,\mathrm{d}\left[|S(j\omega)|^{\circ 2}\right]\Phi_{\mathrm{VM}}(\omega)\,\mathrm{d}\omega \tag{34}$$

where $\mathrm{d}\left[|S(j\omega)|^{\circ 2}\right] \in \{f | f : \mathbb{R}_+ \to \mathbb{R}^{n_y \times n_y}\}$ is a matrix of functions which represent the direction in which the derivative is taken, and $\frac{\partial\lambda_m}{\partial|S(j\omega)|^{\circ 2}} : \{f | f : \mathbb{R}_+ \to \mathbb{R}^{n_y \times n_y}\} \to \mathbb{R}^{n_y}$ maps a direction in the space of matrices of magnitude squared of sensitivity functions evaluated in frequency to a direction in the space of PSD moments.

Equation (34) makes more sense when the sensitivity function is parameterized by parameters $p \in \mathbb{R}^{n_p}$, in which case the chain rule can be applied yielding:

$$\frac{\partial\lambda_m}{\partial p} = \frac{\partial\lambda_m}{\partial|S(j\omega;p)|^{\circ 2}}\frac{\partial|S(j\omega;p)|^{\circ 2}}{\partial p} \tag{35}$$

The adjoint matrix-free directional derivative can be readily calculated by transposition:

$$\left(\frac{\partial\lambda_m}{\partial|S(j\omega)|^{\circ 2}}\right)^{*}\mathrm{d}\lambda_m = \int_{\omega=0}^{\infty} \omega^m \Phi_{\mathrm{VM}}(\omega)^{\top}\,\mathrm{d}\lambda_m\,\mathrm{d}\omega \tag{36}$$

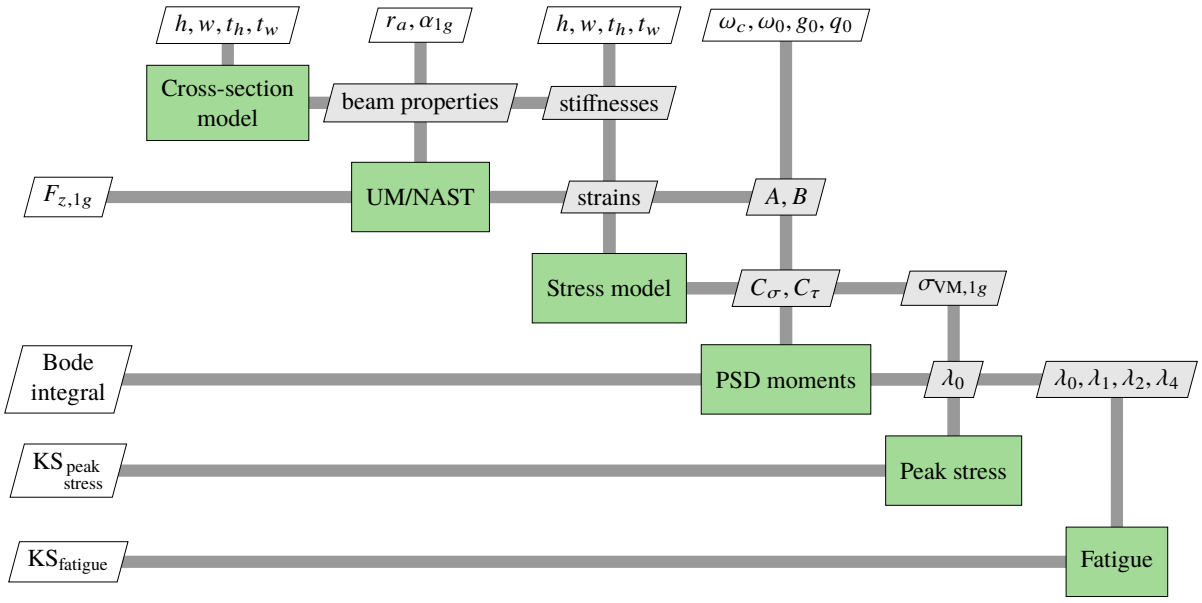

Fig. 2 XDSM diagram showing the information flow for the calculation of the proposed gust metrics

IV. Optimization problem

A. Statement of the problem

In order to illustrate the integration of the proposed combination of sensitivity function parameterization, gust stress constraints (both peak and fatigue), and Bode integral constraint, a simplified wingbox optimization problem is considered. The uniform rectangular wingbox is parameterized in terms of its height, h, width w, side surfaces thickness, t_h, upper and lower surfaces thickness, t_w, and distance between the airfoil leading edge and the reference axis of the wingbox normalized by the chord, r_a, which is defined as the geometric center of the rectangle. In particular, if $r_a = 0$ then the reference axis is located at the leading edge and if $r_a = 1$ then it is located at the trailing edge.

The sensitivity function is parameterized considering a series arrangement of a second-order Butterworth high-pass filter and a peaking filter. It is defined by

$$S(s) = \underbrace{\frac{s^2}{s^2 + \sqrt{2}\omega_c s + \omega_c^2}}_{\text{high-pass filter}} \underbrace{\frac{s^2 + g_0\omega_0 s/q_0 + {\omega_0}^2}{s^2 + \omega_0 s/q_0 + {\omega_0}^2}}_{\text{peaking filter}} \tag{37}$$

The design variables of the sensitivity function are the high-pass filter's cutoff frequency ω_c, and the peaking filter's gain g_0, center frequency ω_0, and quality factor q_0.

For the proposed parameterization, the peak of the magnitude of the sensitivity function bounded by the value of g_0, *i.e.*. $M_S \leq \max(1, g_0)$. Therefore, g_0 is constrained (via a bound in the optimizer) to be less or equal to 2 to ensure the robustness margins mentioned in Section III.B.

Additionally, the trim angle-of-attack, α_{1g}, is included as a design variable to find the equilibrium point around which the system is linearized to obtain the state space representation used in the calculations of the peak gust stress, fatigue, and flutter metrics described in Section II.

The objective is to minimize the wingbox mass, which is calculated by multiplying the cross-sectional mass by the length of the wingbox, L.

The aircraft model chosen for this study is a free-flying blended wing-body (BWB) configuration shown in Figure 3, which is simulated using the University of Michigan's Nonlinear Aeroelastic Simulation Toolbox (UM/NAST) [36]. The simple aeroelastic representation is composed of a geometrically exact, strain-based, beam structural model with strip theory aerodynamics. The BWB model consists of three rigid elements with an 80-kg concentrated mass at the

nose (the body) and 8 flexible elements with parameterized distributed mass and stiffness (the wing). The aerodynamic coefficients along the span are computed based on the local effective angle of attack using a lookup table for the NACA0012 airfoil. Unsteady aerodynamic effects are considered using the 2D Peters' theory [37]. This model was previously used for aeroelastic optimization studies in [38]

The calculation process of the constraints is represented graphically in Figure 2, making use of the eXtended Design Structure Matrix (XDSM) diagram [39]. First the equivalent beam properties (in the strain basis) of the parameterized cross section are calculated using standard formulae (see, *e.g.*, [25]). These properties are the axial stiffness, the torsional stiffness, the in- and out-of-plane bending stiffnesses, the mass linear density and the moments of inertia linear densities. These, along with α_{1g} and r_a, are then input into UM/NAST for the calculation of the residual vertical force $F_{z,1g}$, which is used to inform a trim constraint, and for the calculation of the 1-g strains which are input into the stress model described in Section IV.B to calculate the 1g von Mises aggregated stress $\sigma_{\text{VM, 1g}}$ for the points of interest (which are also described in Section IV.B). The vertical gust to strain system is linearized using algorithmic differentiation (AD) [40] to yield the state space matrices A and B. The stress model is also linearized using AD to obtain the linear relations from strains to normal and shear stresses at the points of interest, C_σ and C_τ. The state space representation thus obtained is then used to calculate the moments of the von Mises stress PSD using (7), modified to account for the designed sensitivity function as shown in (29). The left hand side of Bode integral relation is also computed.

The integrals involved in these calculations are computed numerically using the trapezoidal rule with 400 equally spaced points and truncated to the interval $\omega \in [0.001, 50]$Hz. The truncation to this finite interval avoids numerical challenges with infinite integration intervals and with the poles at the origin present in the UM/NAST linearized system due to the states representing the aircraft reference frame position in space, its heading, and the use of quaternions for attitude representation.

The moments of the stress PSDs are used to compute the the log expected fatigue life, as described in Section II.D, and, combined with the 1g stresses, the margin of safety peak gust stresses (Section II.C) at the points of interest. The values thus obtained are aggregated using the Kreisselmeier-Steinhauser (KS) function [27–29]

$$\text{KS}(g, \rho) = \frac{1}{\rho} \log \sum_j e^{\rho g_j} \tag{38}$$

where g is the vector of constraints to be aggregated and ρ is a positive aggregation parameter. The use of the KS function is motivated by the useful property that it is smooth and approximates the maximum function, in the sense that $\lim_{\rho\to\infty} \text{KS}(g, \rho) = \max(g)$. The following aggregated constraints are considered:

$$\text{KS}_{\text{peak stress}} = \text{KS}(-\text{MS}, 100) \tag{39}$$

$$\text{KS}_{\text{fatigue}} = \text{KS}(\log_{10}[\text{design fatigue life}] - \log_{10}\mathbb{E}[\text{fatigue life}], 100) \tag{40}$$

The choice of the aggregation parameter ρ tries to balance the smoothness of the KS-function with overconservativeness.

Although not shown in Figure 2, the eigenvalues of the A matrix are calculated and used to inform a flutter metric as described in Section II.E:

$$\text{KS}_{\text{flutter}} = \text{KS}(\Re(\text{diag}\,\Lambda) - \mathbf{1} \cdot \text{threshold}, 100) \tag{41}$$

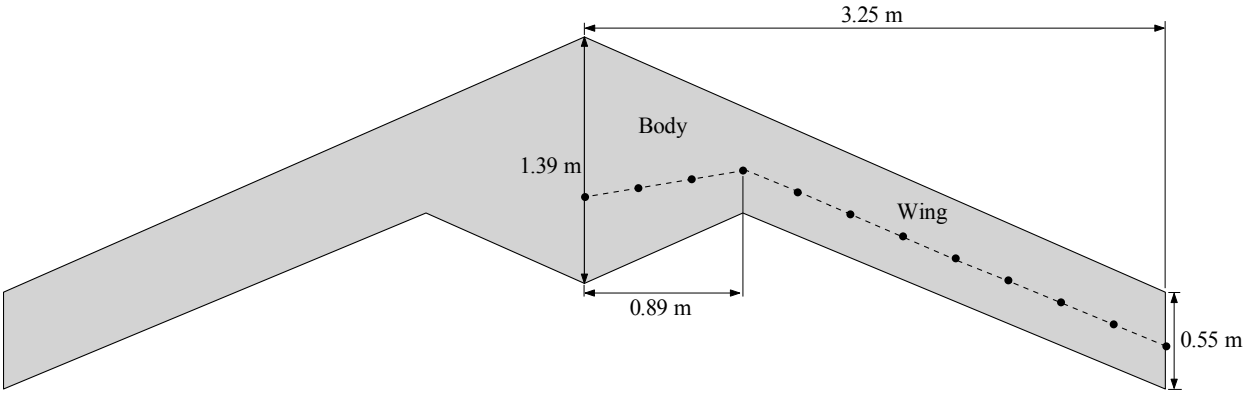

Fig. 3 BWB model planform (dashed line: beam reference axis; markers: beam element ends).

where $\Re(\text{diag}\,\Lambda)$ is a vector containing the real part of the eigenvalues of A, $\mathbf{1}$ is a vector of ones of appropriate size and threshold is a small number of allowable positive damping to compensate for the conservativeness introduced by the KS function combined with the aforementioned eigenvalues at the origin.

Finally, the packaging constraints described in Section IV.C are imposed. They consist of the distance that the wingbox extends vertically over the airfoil outer mold line, for both the fore and aft corners, denoted respectively $\hbar_{\text{fore}}$ and $\hbar_{\text{aft}}$. Only the upper surface is considered since both the airfoil and the wingbox cross sections are symmetric.

The complete problem is stated as follows, and relevant parameters are given in Table 2.

$$
\begin{aligned}
\text{minimize} \quad & 4\rho(t_h h + t_w w)L && \text{(wingbox mass)} && \text{(42a)}\\
\text{with respect to} \quad & h, w, t_h, t_w, r_a, \alpha_{1\text{g}} && \text{(physical design variables)} && \text{(42b)}\\
& \omega_c, \omega_0, g_0, q_0, && \text{(sensitivity function design variables)} && \text{(42c)}\\
\text{subject to} \quad & \text{KS}_{\text{peak stress}} \leq 0 && \text{(peak gust stress constraint)} && \text{(42d)}\\
& \text{KS}_{\text{fatigue}} \leq 0 && \text{(fatigue constraint)} && \text{(42e)}\\
& \text{KS}_{\text{flutter}} \leq 0 && \text{(flutter constraint)} && \text{(42f)}\\
& F_{\text{z,1g}} = 0 && \text{(trim constraint)} && \text{(42g)}\\
& \int_{\omega_{\min}}^{\omega_{\max}} \log|S(j\omega)|\,\mathrm{d}\omega = 0 && \text{(Bode integral relation constraint)} && \text{(42h)}\\
& \hbar_{\text{fore}} \leq 0 && \text{(fore packaging constraint)} && \text{(42i)}\\
& \hbar_{\text{aft}} \leq 0 && \text{(aft packaging constraint)} && \text{(42j)}
\end{aligned}
$$

Table 2 Optimization parameters

Parameter	Value	Source
Flight speed	120 m/s	Design requirements
Flight Altitude	20000 ft	
Threshold (flutter)	0.07	
Design fatigue life	100 000 h	
Turbulence scale	2500 ft	Typical choice for altitude
Fatigue gust intensity	10 ft/s	MIL-STD-1797A
Peak gust intensity	70 ft/s	Hoblit [16]
Young's modulus	70 GPa	Aluminum 7075-T6
Density (ρ)	2700 kg/m^3	
Shear modulus	26 GPa	
$\sigma_{\text{allowable}}$	430 MPa	
k	5.80	MIL-HDBK-5J p. 3-409 Fig. 3.7.6.1(d)
$\log_{10} C$	14.86 $\sqrt[k]{\text{ksi}}$	
$\omega_{\min}$	0.001 Hz	Representative range for this aircraft
$\omega_{\max}$	50 Hz	

This MDO problem was implemented in the OpenMDAO optimization framework [41] and solved using SciPy's SLSQP optimizer.[†]

B. Stress calculation

Usually, the stress constraint used for maneuver loads in high-fidelity static aerostructural optimization is derived from the von Mises stress (or an equivalent for composite constructions) of the wingbox walls at various points along

[†] https://scipy.org

the span [42]. To obtain a similar metric from a beam based model, it is necessary to reintroduce information about the wingbox cross section, which was lost during the condensation process. Hence, a simplified stress model, previously used in [43], is described in what follows.

From the Euler-Bernoulli beam formulation for isotropic material, the normal stress due to bending at a given spanwise station and at a point (x, z) in the cross section is given by

$$\sigma_y = E[\kappa_x z - \kappa_z x] \tag{43}$$

where E is the Young's modulus of the material and κ_x and κ_z are the out-of-plane and in-plane bending curvatures, respectively.

The shear stresses are calculated based on the cross section shear flow. First, the shear flow q_ξ is divided into the basic shear flow $q_{\xi,b}$ and closed-section shear flow $q_{\xi,0}$, so that

$$q_\xi = q_{\xi,b} + q_{\xi,0} \tag{44}$$

The basic shear flow is obtained by introducing a fictitious cut in the upper right corner of the idealized wingbox:

$$q_{\xi,b}(\xi) = \int_0^\xi \left(-\frac{V_x I_{xx} - V_z I_{xz}}{I_{xx} I_{zz} - I_{xz}^2} x(\xi) + \frac{V_z I_{zz} - V_x I_{xz}}{I_{xx} I_{zz} - I_{xz}^2} z(\xi) \right) t(\xi)\, \mathrm{d}\xi, \quad \xi \in [0, 2(w+h)] \tag{45}$$

where ξ is the coordinate that parameterizes the cross section shape by arc length, V_x and V_y are the shear force resolved in the cross sectional local coordinate frame, and I_{xx}, I_{zz}, I_{xz} are the moments of area of the cross section. These moments are obtained by dividing the stiffness matrix of the condensed beam model by the material Young's modulus and not by a direct calculation from the cross section shape.

Finally, the closed-section shear flow is obtained by enforcing the relation between shear flow and torsion, *i.e.*,

$$\kappa_y = \frac{1}{2whG} \oint \frac{q(\xi)}{t(\xi)}\, \mathrm{d}s \tag{46}$$

Applying this relation to the idealized cross section and solving for $q_{\xi,0}$ yields

$$q_{\xi,0} = 2whG\kappa_y \frac{\oint q_{\xi,b}(\xi)/t(\xi)\, \mathrm{d}\xi}{\oint 1/t(\xi)\, \mathrm{d}s} \tag{47}$$

Then the shear stresses in each skin are obtained from the shear flow by the relation

$$\tau = \frac{q_\xi}{t} \tag{48}$$

Integrals (45) to (47) were solved analytically using the symbolic algebra system SymPy[‡] and the resulting closed form solution for shear stress was sampled at the corners and the center of each wall, resulting in a total of 12 points for each cross section. These points are chosen because they are at the extrema of the piecewise parabolic distribution of shear stress that results from this calculation. Eight different cross sections were considered, corresponding to the root of the beam elements used in the UM/NAST model.

Due to the symmetries of the parameterization, the stress value at some of the points will be repeated, but the amount of points was not changed in order to demonstrate the capacity of the approach to handle many sampling points for stress.

These sampled values are then combined with the normal stress from (43) using the von Mises criterion:

$$\sigma_{\mathrm{VM}} = \sqrt{\sigma_y^2 + 3\tau^2} \tag{49}$$

C. Packaging constraint

The shape and position of the rectangular wingbox are also used as design variables, namely the wingbox height h, width w, and the distance of its geometric center to the leading edge of the airfoil, denoted by r_a. It is, therefore, necessary to define constraints that ensure that the wingbox cross section fits inside the airfoil.

[‡] https://www.sympy.org

A symmetric airfoil is fully defined by a function that maps the chord to the thickness, *i.e.*, $t_c(x/c) : [0, 1] \to \mathbb{R}$, where t is the airfoil thickness, c is its chord and x is the coordinate that runs along the chord. For a NACA0012 airfoil, this function is

$$t_c(x/c) = 0.12/0.20[0.2969\sqrt{x/c} - 0.1260x/c - 0.3516(x/c)^2 + 0.2843(x/c)^3 - 0.1015(x/c)^4] \tag{50}$$

The chordwise limits of the wingbox parameterized as described above are $x = r_a \pm w/2$, both at a perpendicular distance of $h/2$ from the chord. The vertical excesses of these two points, normalized by the chord, are then given by

$$\hbar_{\text{fore}} \triangleq \frac{h}{2c} - t_c(r_a - \tfrac{w}{2c}) \tag{51}$$

$$\hbar_{\text{aft}} \triangleq \frac{h}{2c} - t_c(r_a + \tfrac{w}{2c}) \tag{52}$$

Furthermore, the linear constraints $r_a - \frac{w}{2c} \geq 0.05$ and $r_a + \frac{w}{2c} \leq 0.8$ are included to prevent computing t_c outside of the interior of its domain, where it is differentiable. The derivatives of these constraints are calculated using the complex-step method [44] for precision and ease of implementation.

V. Results

A. Verification of derivatives of the proposed gust analysis

In order to numerically verify the procedure for derivative calculation described in Sections II and III, the total derivatives of the proposed constraints with respect to the design variables were calculated using the adjoint method for the arbitrary design point given by: $h = 55\,\text{mm}$, $w = 165\,\text{mm}$, $t_h = 1.0\,\text{mm}$, $t_w = 1.0\,\text{mm}$, $r_a = 0.30$, $\alpha_{1g} = 1.0\,\text{deg}$, $\omega_c = 0.002\,\text{Hz}$, $\omega_0 = 8.0\,\text{Hz}$, $g_0 = 2.0$, $q_0 = 3.0$. These total derivatives were then compared against ones calculated using finite differences (Table 3) and using the direct method (Table 4). For the case of the flutter metric, $\text{KS}_{\text{flutter}}$, the derivatives calculated using the direct method were also included in Table 3 due to the poor matching between direct and adjoint analytical derivatives. A relative step size of $1 \cdot 10^{-6}$ was used when computing the forward finite differences.

The derivative of $\text{KS}_{\text{flutter}}$ had a poor match between the finite differences approximation, and also between the direct and adjoint calculations. The sign of the derivative agrees, but it often has no significant digits in agreement. It is known from the literature [45, 46] that the spectral abscissa (maximum real part of the eigenvalues) is a differentiable function almost everywhere, with the singularity points being where the eigenvalue with the largest real part (the "active" eigenvalue) changes and where there are repeated eigenvalues. The use of the KS aggregation deals with the first issue but not with the second. The steps in the proposed calculation of $\text{KS}_{\text{flutter}}$ (Section II.E) were verified for small random matrices (30×30), and good agreement was obtained.

For the other constraints, there were at least two significant digits in agreement between the derivatives obtained using finite differences and the ones obtained using the adjoint method, which was deemed satisfactory given the loss of precision inherent to finite difference schemes. Agreement of approximately ten significant digits was obtained between the direct and adjoint calculation of the derivatives.

A more qualitative form of derivative verification is presented in Figure 4 for the flutter metric and Figure 5 for the other gust metrics. These figures plot sweeps in r_a of the functions of interest in which the base of the arrow marks the function value at each point and the tip of each arrow is at the linear approximation for the next sampled point. Therefore, for a linear function, the tip of one arrow should touch the base of the next arrow, and, for a function with mild non-linearities, they should be close. The functions in Figure 5 are smooth especially in the stable region, $r_a < 0.8$, as is the behavior of the individual eigenvalues shown in Figure 4b. However, the aggregated flutter metric, shown in Figure 4a shows strong non-linearities due to the eigenvalues close to the origin contributing the most to the aggregated value until very close to flutter, when the "active" eigenvalue changes and this causes a sharp change in the slope of $\text{KS}_{\text{flutter}}$.

B. Optimization results

Two simplified versions of the optimization problem proposed in (42) converged successfully to a tolerance of $1 \cdot 10^{-6}$, both in open-loop ($S(j\omega) = 1\ \forall\omega$) and in closed-loop ($S(j\omega)$ given by (37)). They are summarized in Table 5, which shows an over five times increase in computational cost when the sensitivity function is designed. This suggests that the parameterization of the sensitivity function proposed leads to a hard optimization problem.

Table 3 Verification of exact derivatives against finite differences (not matching digits are underlined)

(a) Derivatives with respect to physical variables

of	wrt mode	h (m)	w (m)	t_h (mm)	t_w (mm)	r_a (chord fr.)	α_{1g} (deg)
$KS_{\substack{\text{peak}\\\text{stress}}}$	Adjoint	-50.13202772	-14.33102859	-0.41305936	-2.08192256	2.49292277	0.29274164
	FD	-50.10366989	-14.32064796	-0.41284357	-2.08149928	2.49432521	0.28969245
$KS_{fatigue}$	Adjoint	-67.02255179	-19.10264589	-0.47102252	-2.90887711	3.68266921	0.03308077
	FD	-66.97753730	-19.08519747	-0.47072755	-2.90829519	3.68514846	0.02794816
$KS_{flutter}$	Adjoint	0.02622839	0.00431653	0.00010136	0.00066053	-0.00117842	-0.00026081
	Direct	0.01871342	0.00288407	0.00006185	0.00047869	-0.00107073	-0.00013206
	FD	0.01906667	0.00288560	0.00005308	0.00047050	-0.00105289	-0.00207511
$F_{z,1g}$ (kN)	Adjoint	-0.36771291	-1.31224912	-0.07095762	-0.03193474	0.61907804	1.69712136
	FD	-0.36771793	-1.31224835	-0.07095741	-0.03193466	0.61907809	1.69712117

(b) Derivatives with respect to control-related variables

of	wrt mode	ω_c (rad/s)	ω_0 (rad/s)	g_0 (-)	q_0 (-)
$KS_{peak\ stress}$	Exact	-0.00009598	-0.00494446	0.09541288	-0.04261832
	FD	-0.00009597	-0.00494445	0.09541291	-0.04261827
$KS_{fatigue}$	Exact	-0.00010181	-0.00967206	0.18211993	-0.07998246
	FD	-0.00010180	-0.00967300	0.18212893	-0.07998605
Bode integral	Exact	-58.96978592	0.46865546	24.50766684	-7.86823638
	FD	-58.96976280	0.46865543	24.50766594	-7.86822896

Table 4 Relative errors between direct and adjoint derivatives

(a) With respect to physical variables

wrt of	h (m)	w (m)	t_h (mm)	t_w (mm)	r_a (chord fr.)	α_{1g} (deg)
$KS_{peak\ stress}$	$-1.7 \cdot 10^{-12}$	$-3.4 \cdot 10^{-11}$	$-3.5 \cdot 10^{-11}$	$-7.5 \cdot 10^{-12}$	$-1.7 \cdot 10^{-10}$	$5.7 \cdot 10^{-14}$
$KS_{fatigue}$	$2.1 \cdot 10^{-12}$	$1.5 \cdot 10^{-11}$	$2.6 \cdot 10^{-11}$	$3.3 \cdot 10^{-12}$	$1.1 \cdot 10^{-10}$	$1.9 \cdot 10^{-13}$
$KS_{flutter}$	$-2.9 \cdot 10^{-1}$	$-3.3 \cdot 10^{-1}$	$-3.9 \cdot 10^{-1}$	$-2.8 \cdot 10^{-1}$	$-9.1 \cdot 10^{-2}$	$-4.9 \cdot 10^{-1}$

(b) With respect to control-related variables

wrt of	ω_c (rad/s)	ω_0 (rad/s)	g_0 (-)	q_0 (-)
$KS_{peak\ stress}$	0.0	0.0	$1.3 \cdot 10^{-15}$	$-1.1 \cdot 10^{-15}$
$KS_{fatigue}$	$-4.0 \cdot 10^{-16}$	$-1.8 \cdot 10^{-16}$	0.0	$-6.9 \cdot 10^{-16}$

Note: 0.0 indicates identical 64-bit floating point representations

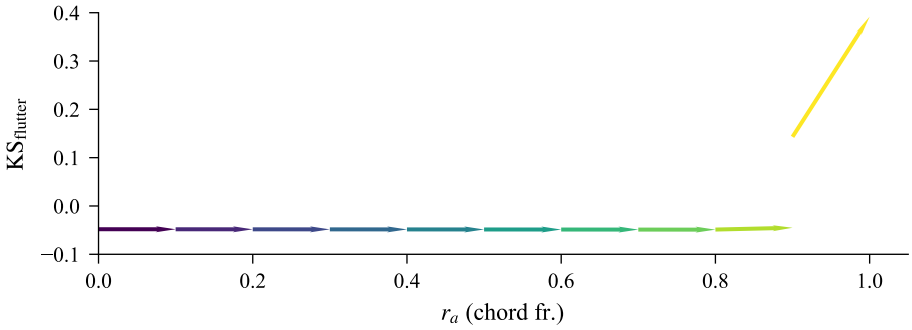

(a) KS-aggregated flutter constraint

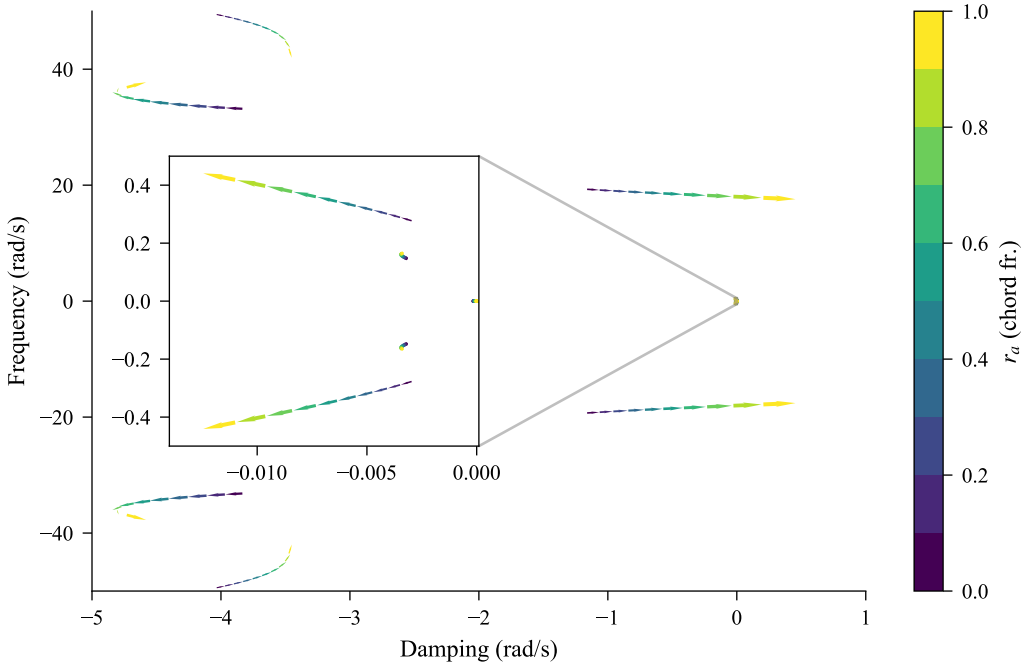

(b) Root locus. An inset zooming in on the roots close to the origin was added

Fig. 4 Flutter metric with derivatives for varying relative position of the airfoil and wingbox

Table 5 Optimization problems solved

	Design variables		Constraint	# Evaluations	
Case	h, w, r_a	$\omega_c, \omega_0, g_0, q_0$	$\text{KS}_{\text{flutter}}$	Function	Jacobian
A			✓	6	6
B		✓	✓	42	32
C	✓			13	10
D	✓	✓		85	64

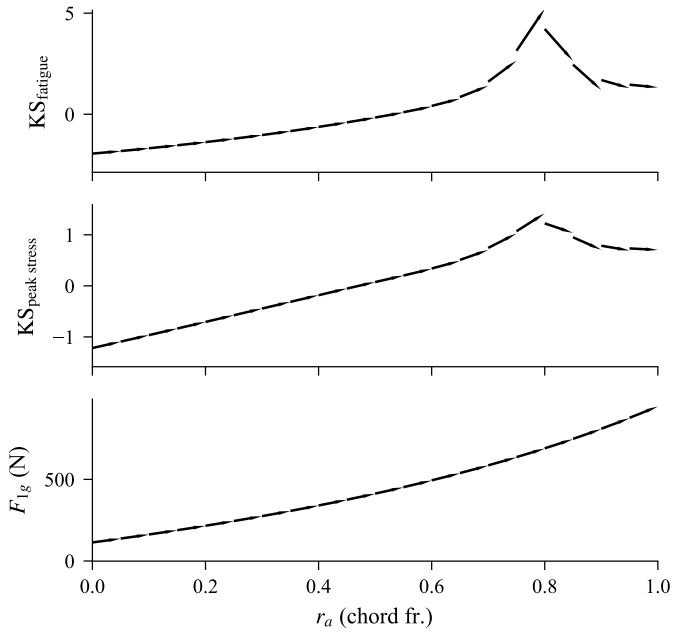

Fig. 5 Parametric study of the gust stress and trim constraints with varying relative position between the wingbox and the airfoil

Table 6 Optimization results for problem with fixed wingbox shape (A,B)

(a) Design variables

	Open-loop design	Closed-loop design	Δ [%]	Lower bound	Upper bound
t_h (mm)	0.657	0.456	−30.6%	0.100	2.000
t_w (mm)	0.851	0.455	−46.5%	0.100	2.000
α_{1g} (deg)	0.811	0.790	−2.6%	−10.00	10.000
ω_c (Hz)	-	5.000	-	0.000	5.000
ω_0 (Hz)	-	10.00	-	5.000	10.000
g_0 (-)	-	2.000	-	1.000	2.000
q_0 (-)	-	1.139	-	1.000	10.000

(b) Response variables

	Open-loop design	Closed-loop design	Δ [%]	Lower bound	Upper bound
$KS_{\text{peak stress}}$	$1.1 \cdot 10^{-8}$	$1.0 \cdot 10^{-7}$	-	-	0
KS_{flutter}	−0.048	-0.048	-	-	0
KS_{fatigue}	−0.346	−0.938	-	-	0
$F_{z,1g}$ (N)	$3.5 \cdot 10^{-7}$	$-3.2 \cdot 10^{-6}$	-	0	0
Bode integral	-	$-8.5 \cdot 10^{-14}$	-	0	0
Mass (kg)	2.591	1.470	−43.3%	-	-

Table 7 Optimization results for problem without the flutter constraint (C, D)

(a) Design variables

	Open-loop design	Closed-loop design	Δ [%]	Lower bound	Upper bound
h (m)	0.061	0.050	−18.0%	0.027	0.066
w (m)	0.159	0.092	−42.1%	0.005	0.549
t_h (mm)	0.590	0.522	−11.5%	0.100	2.000
t_w (mm)	0.807	0.563	−22.2%	0.100	2.000
r_a (chord fr.)	0.315	0.175	−30.2%	0.100	2.000
α_{1g} (deg)	0.796	0.785	−1.4%	−10.00	10.000
ω_c (Hz)	-	7.451	-	0.000	10.000
ω_0 (Hz)	-	15.00	-	10.000	15.000
g_0 (-)	-	2.000	-	1.000	2.000
q_0 (-)	-	1.000	-	1.000	10.000

(b) Response variables

	Open-loop design	Closed-loop design	Δ [%]	Lower bound	Upper bound
$\mathrm{KS}_{\text{peak stress}}$	$4.9 \cdot 10^{-8}$	$1.6 \cdot 10^{-7}$	-	-	0
$\mathrm{KS}_{\text{fatigue}}$	−0.354	−2.157	-	-	0
$F_{z,1g}$ (N)	$6.5 \cdot 10^{-6}$	$-4.2 \cdot 10^{-5}$	-	0	0
Bode integral	-	$-8.5 \cdot 10^{-14}$	-	0	0
$\hbar_{\text{fore}}$ (chord fr.)	$1.8 \cdot 10^{-13}$	$2.0 \cdot 10^{-8}$	-	-	0
$\hbar_{\text{aft}}$ (chord fr.)	$1.2 \cdot 10^{-13}$	−0.014	-	-	0
Mass (kg)	2.421	1.144	−52.7%	-	-

The first simplified version of the optimization problem (cases A and B) includes all constraints but drops the design variables that position shape the wingbox, *i.e.*, h, w, and r_a. These variables are fixed at the values described in Section V.A. The optimum design and response for this version of the problem are shown in Table 6. The second version of the problem (cases C and D) includes all the design variables but drops the flutter constraint, $\mathrm{KS}_{\mathrm{flutter}}$. The optimum design and response for this version of the problem are shown in Table 7. Adding the design variables for the wingbox shape caused a reduction in mass for the open-loop designs (*i.e.*, between cases A and C) of 6.6%. Cases B and D are not directly comparable because of changes in the bounds for ω_c and ω_0, which corresponds to different assumed bandwidths for the control systems.

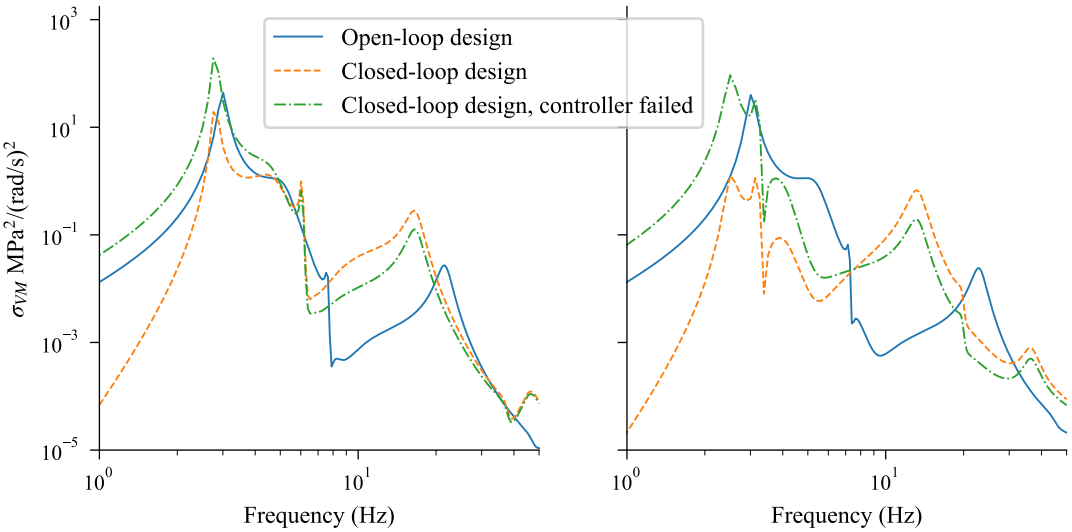

(a) Optimal design with wingbox shape fixed (A, B)

(b) Optimal design without the flutter constraint (C, D)

Fig. 6 Stress PSD for the critical point in peak stress

Figure 6 shows the von Mises stress PSD for the optimal designs found. The closed-loop design exhibits a reduction in the first peak in the PSD (around 2 Hz) thanks to the sensitivity function, which in turn allows the peak between 10–20 Hz to be moved closer to 10 Hz, where the von Kármán PSD has more energy and therefore makes the peak higher, while maintaining the same level of peak stress.

In all cases the peak stress constraint is active while the fatigue constraint is not, despite the stress having greater magnitudes at higher frequencies for the closed-loop cases (B and D). The open-loop poles for the various designs are shown in Figure 7. Designs A, B, and C are open-loop stable but D is not. This highlights the desirability of including the flutter constraint in the problem.

C. Sensitivity analysis

Since the Jacobian of the optimization problems is readily available, a sensitivity analysis was conducted at the optimum and the results are shown in Tables 8 and 9, normalized by the optimum value of the design variables (denoted by an $\star$ superscript. These figures are color coded based on the value of the derivatives, with stronger shades of reds denoting larger positive values and shades of blue denoting negative values.

These derivatives show that an increase in the dimensions of the wingbox causes reduction of peak stress and increase in mass. However, increasing the height and width of the wingbox decreases the fatigue damage in the open-loop optimum design of case C, but mildly increases it in the closed-loop optimum design of case D. This is likely due to the competing effects that increasing stiffness shifts the stresses to higher frequencies, while adding material decreases the stresses in all frequencies. Moving the wingbox towards the leading edge is favorable for both peak stresses and fatigue metrics. Finally, the flutter metric is largely insensitive to changes in the design because the designs A and B are flutter-free, and therefore the eigenvalues with largest real part are the ones fixed at the origin, related to the position and heading of the aircraft reference frame, and they dominate the KS aggregation.

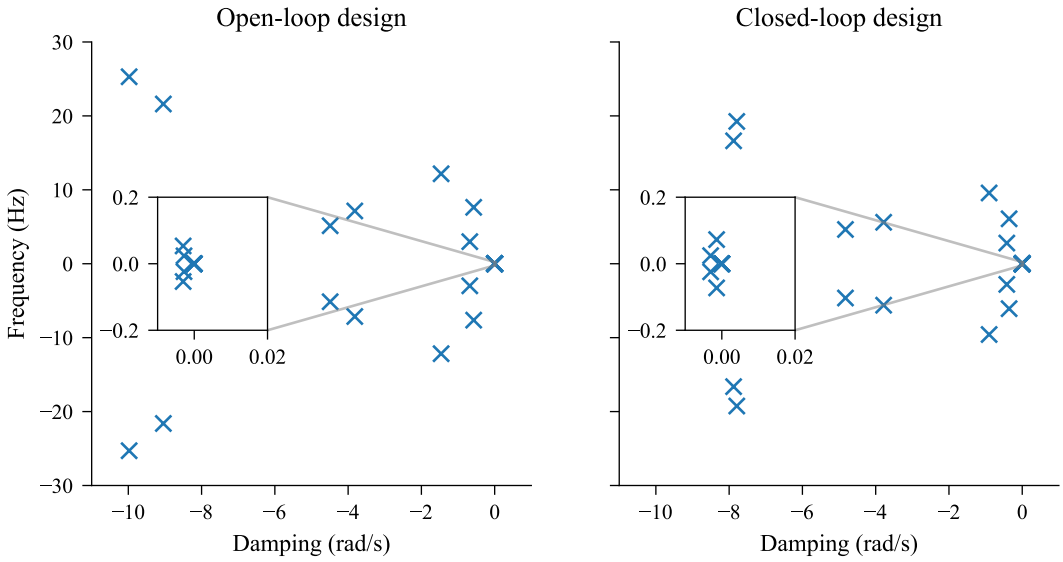

(a) Optimal design with fixed wingbox shape (A, B)

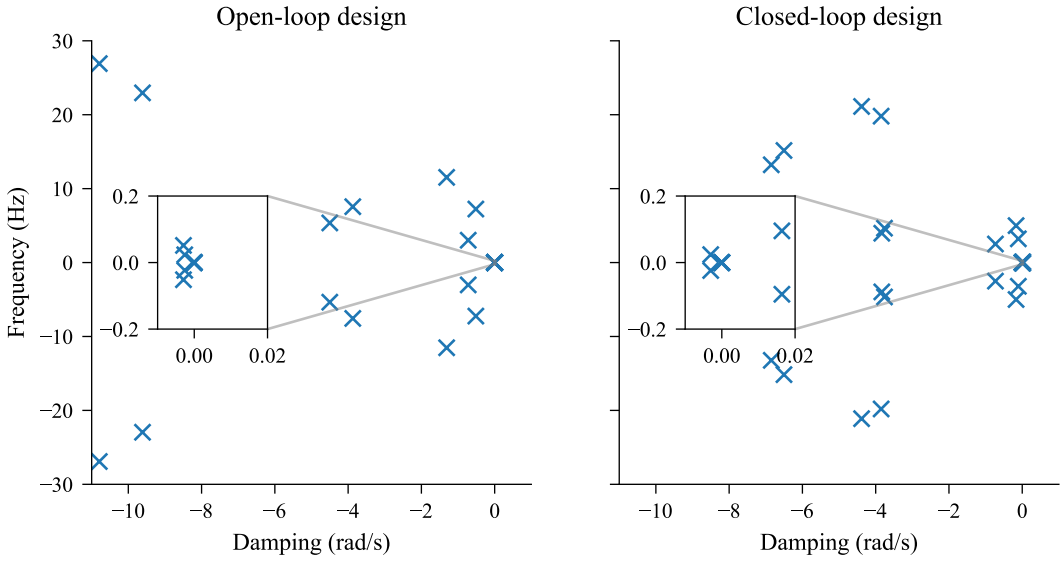

(b) Optimal design without the flutter constraint (C, D)

Fig. 7 Pole map for the different designs, with insets zooming in close to the origin

Table 8 Derivatives at the optimum point with fixed wingbox shape

(a) Open-loop design (case A)

w.r.t. of	$t_h/t_h^\star$	$t_w/t_w^\star$	$\alpha_{1g}/\alpha_{1g}^\star$
$KS_{\text{dynamic stress}}$	−0.422	−1.594	0.164
KS_{fatigue}	−0.450	−2.990	0.031
KS_{flutter}	0.000	0.000	0.000
$F_{z,1g}$ (kN)	−0.107	−0.026	1.341
Mass (kg)	0.530	2.061	0.000

(b) Closed-loop design (case B)

w.r.t. of	$t_h/t_h^\star$	$t_w/t_w^\star$	$\alpha_{1g}/\alpha_{1g}^\star$
$KS_{\text{dynamic stress}}$	−0.392	−1.128	0.216
KS_{fatigue}	−0.547	−1.798	0.031
KS_{flutter}	0.000	−0.001	0.000
$F_{z,1g}$ (kN)	−0.078	0.034	1.197
Mass (kg)	0.368	1.103	0.000

w.r.t. of	$\omega_c/\omega_c^\star$	$\omega_0/\omega_0^\star$	$g_0/g_0^\star$	$q_0/q_0^\star$
$KS_{\text{dynamic stress}}$	−1.229	−0.139	0.321	−0.178
KS_{fatigue}	−3.252	−0.273	1.037	−0.543
Bode integral	−69.755	57.538	135.074	−58.296

Table 9 Derivatives at the optimum point without the flutter constraint

(a) Open-loop design (case C)

w.r.t. of	$h/h^\star$	$w/w^\star$	$t_h/t_h^\star$	$t_w/t_w^\star$	$r_a/r_a^\star$	$\alpha_{1g}/\alpha_{1g}^\star$
$\mathrm{KS}_{\text{dynamic stress}}$	−2.505	−2.130	−0.478	−1.665	0.846	0.169
$\mathrm{KS}_{\text{fatigue}}$	−4.391	−3.648	−0.522	−3.185	1.596	0.036
$F_{z,1g}$ (kN)	−0.102	−0.330	−0.129	−0.032	0.210	1.344
Mass (kg)	0.526	1.895	0.526	1.895	0.000	0.000

(b) Closed-loop design (case D)

w.r.t. of	$h/h^\star$	$w/w^\star$	$t_h/t_h^\star$	$t_w/t_w^\star$	$r_a/r_a^\star$	$\alpha_{1g}/\alpha_{1g}^\star$
$\mathrm{KS}_{\text{dynamic stress}}$	−0.835	−0.988	−0.404	−0.732	0.399	0.208
$\mathrm{KS}_{\text{fatigue}}$	0.196	0.227	0.012	−0.768	0.862	0.036
$F_{z,1g}$ (kN)	0.341	−0.230	−0.111	0.142	0.151	1.084
Mass (kg)	0.382	0.762	0.382	0.762	0.000	0.000

w.r.t. of	$\omega_c/\omega_c^\star$	$\omega_0/\omega_0^\star$	$g_0/g_0^\star$	$q_0/q_0^\star$
$\mathrm{KS}_{\text{dynamic stress}}$	−0.347	−0.132	0.340	−0.044
$\mathrm{KS}_{\text{fatigue}}$	−1.430	−0.683	1.958	−0.243
Bode integral	−103.882	65.774	189.270	−70.346

Notably, the open-loop designs (cases A and C) are more sensitive to changes in the structural design variables than the closed-loop designs (cases B and D), supporting the well-known idea that adding feedback control to the system makes its performance less sensitive to variations in the plant.

VI. Conclusion and future work

This paper presented an approach to include stochastic gust constraints for peak stress and fatigue into an MDO problem, complete with matrix-free derivatives for the direct and adjoint (reverse) modes. A constraint for ensuring the stability of the system (*i.e.*, preventing flutter) developed in previous work was used but presented some problems with its derivatives, which were discussed. An approach for including control considerations into the design, without explicitly designing the controller was proposed, and it consists of designing the sensitivity to stress transfer function of the closed-loop system as part of the MDO problem.

A simplified MDO problem was proposed and solved to show the effect of applying the approach. The use of the parameterized sensitivity function was able to reduce the mass of the wing (objective), while still satisfying the other constraints. The need for having a working flutter constraint was highlighted. The sensitivity of the optimum design with respect to changes in the design variables was calculated, and it was shown that the performance of the closed-loop design is more robust to changes in the structural variables.

For future work, the problems with the flutter constraint will be investigated further. The assumption of a uniform wingbox will be dropped, adding distributed design variables to the problem, which will highlight the performance advantage of calculating the derivatives in the adjoint mode. The sensitivity of the optimum design with respect to changes in the constraints will be calculated using the Lagrange multipliers, as well as the sensitivity of the optimum design with respect to changes in the design variables but still respecting the physical constraints, namely the trim and the Bode integral relation.

Bibliography

[1] Suzuki, S., and Yonezawa, S., "Simultaneous Structure/Control Design Optimization of a Wing Structure with a Gust Load Alleviation System," *Journal of aircraft*, Vol. 30, No. 2, 1993, pp. 268–274.

[2] Hunten, K., Zink, S., Flansburg, B., and Engelstad, S., "A Systems MDO Approach for an Unmanned Aerial Vehicle," *48th AIAA/ASME/ASCE/AHS/ASC Structures, Structural Dynamics, and Materials Conference*, American Institute of Aeronautics and Astronautics, 2007. doi:10.2514/6.2007-1877.

[3] Haghighat, S., Martins, J. R. R. A., and Liu, H. H. T., "Aeroservoelastic Design Optimization of a Flexible Wing," *Journal of Aircraft*, Vol. 49, 2012, pp. 432–443. doi:10.2514/1.C031344.

[4] Xu, J., and Kroo, I., "Aircraft Design with Active Load Alleviation and Natural Laminar Flow," *Journal of Aircraft*, Vol. 51, No. 5, 2014, pp. 1532–1545. doi:10.2514/1.c032402.

[5] Stanford, B., "Optimal Aircraft Control Surface Layouts for Maneuver and Gust Load Alleviation," *AIAA Scitech 2020 Forum*, American Institute of Aeronautics and Astronautics, 2020. doi:10.2514/6.2020-0448.

[6] Krengel, M. D., and Hepperle, M., "Gust and Maneuver Load Alleviation in Conceptual Overall Aircraft Design," *AIAA AVIATION 2023 Forum*, American Institute of Aeronautics and Astronautics, 2023. doi:10.2514/6.2023-3369.

[7] Vartio, E., Shaw, E., and Vetter, T., "Gust Load Alleviation Flight Control System Design for a SensorCraft Vehicle," *26th AIAA Applied Aerodynamics Conference*, American Institute of Aeronautics and Astronautics, 2008. doi:10.2514/6.2008-7192.

[8] Zeng, J., Moulin, B., de Callafon, R., and Brenner, M. J., "Adaptive Feedforward Control for Gust Load Alleviation," *Journal of Guidance, Control, and Dynamics*, Vol. 33, 2010. doi:10.2514/1.46091.

[9] Dillsaver, M., Cesnik, C. E. S., and Kolmanovsky, I., "Gust Load Alleviation Control for Very Flexible Aircraft," *AIAA Atmospheric Flight Mechanics Conference*, American Institute of Aeronautics and Astronautics, 2011. doi:10.2514/6.2011-6368.

[10] Haghighat, S., Liu, H. H. T., and Martins, J. R. R. A., "Model-Predictive Gust Load Alleviation Controller for a Highly Flexible Aircraft," *Journal of Guidance, Control, and Dynamics*, Vol. 35, 2012. doi:10.2514/1.57013.

[11] De Freitas Virgilio Pereira, M., "Constrained Control for Load Alleviation in Very Flexible Aircraft," Ph.D. thesis, University of Michigan, 2022. doi:10.7302/6287.

[12] Ting, K.-Y., Mavriplis, N., Soltani, R., Nelson, C. P., and Livne, E., "Supersonic Configurations at Low Speeds (SCALOS): Model Geometry and Aerodynamic Results," *AIAA SCITECH 2022 Forum*, American Institute of Aeronautics and Astronautics, 2022. doi:10.2514/6.2022-1800.

[13] Fournier, H., Massioni, P., Pham, M. T., Bako, L., Vernay, R., and Colombo, M., "Robust Gust Load Alleviation at Different Flight Points and Mass configurations," *AIAA SCITECH 2022 Forum*, American Institute of Aeronautics and Astronautics, 2022. doi:10.2514/6.2022-0285.

[14] Duessler, S., Mylvaganam, T., and Palacios, R., "LQG-based Gust Load Alleviation Systems for Very Flexible Aircraft," *AIAA SCITECH 2023 Forum*, American Institute of Aeronautics and Astronautics, 2023. doi:10.2514/6.2023-2571.

[15] Díaz, J. M., Costa-Castelló, R., and Dormido, S., "Closed-Loop Shaping Linear Control System Design: An Interactive Teaching/Learning Approach [Focus on Education]," *IEEE Control Systems*, Vol. 40, 2019. doi:10.1109/MCS.2019.2925255.

[16] Hoblit, F. M., *Gust Loads on Aircraft: Concepts and Applications*, American Institute of Aeronautics and Astronautics, Reston, Virginia, 1988.

[17] Magnus, J. R., and Neudecker, H., *Matrix Differential Calculus with Applications in Statistics and Econometrics*, 3rd ed., Wiley & Sons, Limited, John, 2019. doi:10.1002/9781119541219.

[18] Preumont, A., and Piéfort, V., "Predicting Random High-Cycle Fatigue Life With Finite Elements," *Journal of Vibration and Acoustics*, Vol. 116, No. 2, 1994, pp. 245–248. doi:10.1115/1.2930420.

[19] Talvila, E., "Necessary and Sufficient Conditions for Differentiating under the Integral Sign," *The American Mathematical Monthly*, Vol. 108, No. 6, 2001, pp. 544–548. URL http://www.jstor.org/stable/2695709.

[20] Palmgren, A., "Die Lev/bensdauer von kugellagern," *VDI. Z.*, Vol. 68, 1924, pp. 339–341.

[21] Miner, M. A., "Cumulative Damage in Fatigue," *Journal of Applied Mechanics*, Vol. 12, No. 3, 1945, pp. A159–A164. doi:10.1115/1.4009458.

[22] Murakami, Y., "What is fatigue damage? A viewpoint from the observation of a low-cycle fatigue process," *Metal Fatigue*, Elsevier, 2019, pp. 643–668. doi:10.1016/b978-0-12-813876-2.00023-6.

[23] Dirlik, T., "Application of computers in fatigue analysis," Ph.D. thesis, University of Warwick, 1985.

[24] Benasciutti, D., and Tovo, R., "Comparison of spectral methods for fatigue analysis of broad-band Gaussian random processes," *Probabilistic Engineering Mechanics*, Vol. 21, No. 4, 2006, pp. 287–299.

[25] Megson, T. H. G., *Aircraft structures for engineering students*, Butterworth-Heinemann, 2016.

[26] Jonsson, E., Riso, C., Monteiro, B. B., Gray, A. C., Martins, J. R. R. A., and Cesnik, C. E. S., "High-Fidelity Gradient-Based Wing Structural Optimization Including Geometrically Nonlinear Flutter Constraint," *AIAA Journal*, Vol. 61, No. 7, 2023, pp. 3045–3061. doi:10.2514/1.J061575.

[27] Kreisselmeier, G., and Steinhauser, R., "Systematic Control Design by Optimizing a Vector Performance Index," *International Federation of Active Controls Symposium on Computer-Aided Design of Control Systems, Zurich, Switzerland*, 1979. doi:10.1016/S1474-6670(17)65584-8.

[28] Wrenn, G. A., "An Indirect Method for Numerical Optimization Using the Kreisselmeier–Steinhauser Function," Tech. Rep. CR-4220, NASA Langley Research Center, Hampton, VA, 1989.

[29] Poon, N. M., and Martins, J. R., "An adaptive approach to constraint aggregation using adjoint sensitivity analysis," *Structural and Multidisciplinary Optimization*, Vol. 34, No. 1, 2007, pp. 61–73.

[30] Nelson, R. B., "Simplified calculation of eigenvector derivatives," *AIAA Journal*, Vol. 14, No. 9, 1976, pp. 1201–1205. doi:10.2514/3.7211.

[31] Bode, H. W., *Network analysis and feedback amplifier design*, Bell Telephone Laboratories series, D. Van Nostrand, 1945.

[32] Freudenberg, J., and Looze, D., "Right half plane poles and zeros and design tradeoffs in feedback systems," *IEEE Transactions on Automatic Control*, Vol. 30, No. 6, 1985, pp. 555–565. doi:10.1109/tac.1985.1104004.

[33] Skogestad, S., and Postlethwaite, I., *Multivariable feedback control: analysis and design*, 2nd ed., John Wiley & Sons, Ltd, 2007.

[34] Li, Y., and Lee, E., "Stability Robustness Characterization and Related Issues for Control Systems Design," *Automatica*, Vol. 29, No. 2, 1993, pp. 479 – 484. doi:https://doi.org/10.1016/0005-1098(93)90142-G, URL http://www.sciencedirect.com/science/article/pii/000510989390142G.

[35] Stein, G., "Respect the unstable," *IEEE Control Systems*, Vol. 23, No. 4, 2003, pp. 12–25. doi:10.1109/mcs.2003.1213600.

[36] Su, W., and Cesnik, C. E. S., "Nonlinear aeroelasticity of a very flexible blended-wing-body aircraft," *Journal of Aircraft*, Vol. 47, No. 5, 2010, pp. 1539–1553. doi:10.2514/1.47317.

[37] Peters, D. A., Hsieh, M. C. A., and Torrero, A., "A State-Space Airloads Theory for Flexible Airfoils," *Journal of the American Helicopter Society*, Vol. 52, No. 4, 2007, pp. 329–342. doi:10.4050/JAHS.52.329.

[38] Rosatelli, P., Cesnik, C. E. S., and Lupp, C. A., "Fuel burn Minimization Including Dynamic Aeroelastic Constraint for Free-flying Vehicle Under Geometrically Nonlinear Deformations," *AIAA SciTech Forum 2023*, National Harbor, MD, 2023. doi:10.2514/6.2023-0729.

[39] Lambe, A. B., and Martins, J. R. R. A., "Extensions to the Design Structure Matrix for the Description of Multidisciplinary Design, Analysis, and Optimization Processes," *Structural and Multidisciplinary Optimization*, Vol. 46, 2012, pp. 273–284. doi:10.1007/s00158-012-0763-y.

[40] Sagebaum, M., Albring, T., and Gauger, N. R., "High-Performance Derivative Computations using CoDiPack," *ACM Transactions on Mathematical Software (TOMS)*, Vol. 45, No. 4, 2019. doi:10.1145/3356900.

[41] Gray, J. S., Hwang, J. T., Martins, J. R. R. A., Moore, K. T., and Naylor, B. A., "OpenMDAO: An Open-Source Framework for Multidisciplinary Design, Analysis, and Optimization," *Structural and Multidisciplinary Optimization*, Vol. 59, 2019, pp. 1075–1104. doi:10.1007/s00158-019-02211-z.

[42] Kenway, G. K., Kennedy, G. J., and Martins, J. R., "Scalable Parallel Approach for High-Fidelity Steady-State Aeroelastic Analysis and Adjoint Derivative Computations," *AIAA journal*, Vol. 52, No. 5, 2014, pp. 935–951.

[43] Bahia Monteiro, B., Gray, A. C., Cesnik, C. E. S., Kolmanovsky, I., and Vetrano, F., "Bi-level Multidisciplinary Design Optimization of a Wing Considering Maneuver Load Alleviation and Flutter," *AIAA SCITECH 2023 Forum*, 2023, p. 0728. doi:10.2514/6.2023-0728.

[44] Martins, J. R. R. A., Sturdza, P., and Alonso, J. J., "The Complex-Step Derivative Approximation," *ACM Trans. Math. Softw.*, Vol. 29, No. 3, 2003, p. 245–262. doi:10.1145/838250.838251, URL https://doi.org/10.1145/838250.838251.

[45] Kato, T., *A Short Introduction to Perturbation Theory for Linear Operators*, Springer US, 1982.

[46] Burke, J. V., and Overton, M. L., "Differential properties of the spectral abscissa and the spectral radius for analytic matrix-valued mappings," *Nonlinear Analysis: Theory, Methods & Applications*, Vol. 23, No. 4, 1994, pp. 467–488. doi:10.1016/0362-546x(94)90090-6.